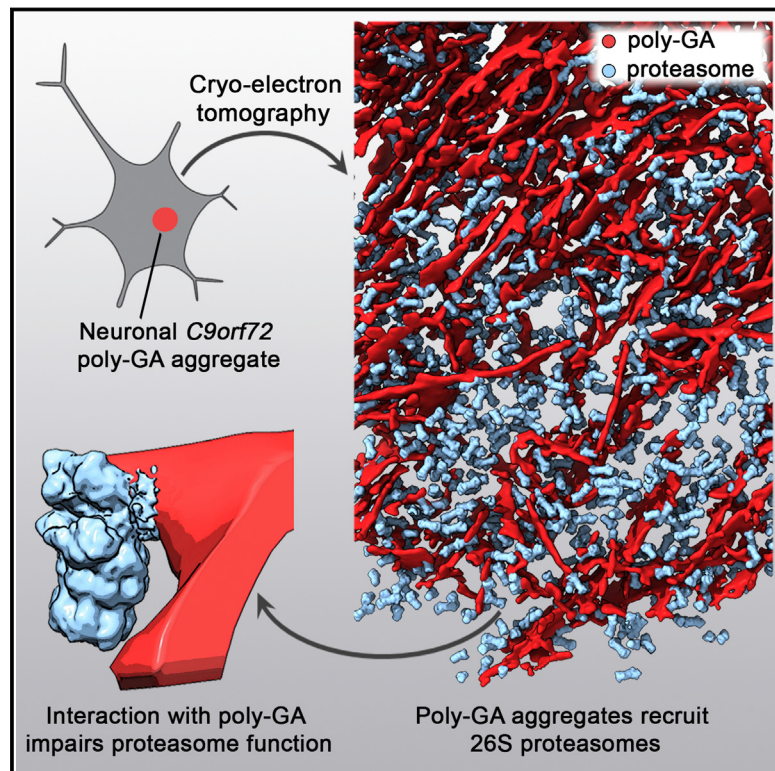


In Situ Structure of Neuronal C9orf72 Poly-GA Aggregates Reveals Proteasome Recruitment

Graphical Abstract



Authors

Qiang Guo, Carina Lehmer,
Antonio Martínez-Sánchez, ...,
Dieter Edbauer, Wolfgang Baumeister,
Rubén Fernández-Busnadio

Correspondence

dieter.edbauer@dzne.de (D.E.),
baumeist@biochem.mpg.de (W.B.),
ruben@biochem.mpg.de (R.F.-B.)

In Brief

Neuronal poly-GA aggregates linked to amyotrophic lateral sclerosis and frontotemporal dementia selectively sequester proteasomes.

Highlights

- Neuronal C9orf72 poly-GA aggregates were analyzed by cryoelectron tomography
- Poly-GA aggregates in neurons consist of planar twisted ribbons
- Poly-GA aggregates recruit proteasomes while excluding other large macromolecules
- Interactions with poly-GA aggregates lead to proteasome stalling



In Situ Structure of Neuronal C9orf72 Poly-GA Aggregates Reveals Proteasome Recruitment

Qiang Guo,¹ Carina Lehmer,^{2,3,8} Antonio Martínez-Sánchez,^{1,8} Till Rudack,^{4,5,8} Florian Beck,¹ Hannelore Hartmann,^{2,3} Manuela Pérez-Berlanga,⁶ Frédéric Frottin,⁶ Mark S. Hipp,^{3,6} F. Ulrich Hartl,^{3,6} Dieter Edbauer,^{2,3,7,*} Wolfgang Baumeister,^{1,9,*} and Rubén Fernández-Busnadiego^{1,*}

¹Department of Molecular Structural Biology, Max Planck Institute of Biochemistry, 82152 Martinsried, Germany

²German Center for Neurodegenerative Diseases (DZNE), 81377 Munich, Germany

³Munich Cluster for Systems Neurology (SyNergy), 80336 Munich, Germany

⁴Department of Biophysics, Ruhr University Bochum, 44780 Bochum, Germany

⁵NIH Center for Macromolecular Modeling and Bioinformatics, Beckman Institute for Advanced Science and Technology, University of Illinois at Urbana-Champaign, Champaign, IL 61801, USA

⁶Department of Cellular Biochemistry, Max Planck Institute of Biochemistry, 82152 Martinsried, Germany

⁷Ludwig-Maximilians University Munich, 81377 Munich, Germany

⁸These authors contributed equally

⁹Lead Contact

*Correspondence: dieter.edbauer@dzne.de (D.E.), baumeist@biochem.mpg.de (W.B.), ruben@biochem.mpg.de (R.F.-B.)

<https://doi.org/10.1016/j.cell.2017.12.030>

SUMMARY

Protein aggregation and dysfunction of the ubiquitin-proteasome system are hallmarks of many neurodegenerative diseases. Here, we address the elusive link between these phenomena by employing cryo-electron tomography to dissect the molecular architecture of protein aggregates within intact neurons at high resolution. We focus on the poly-Gly-Ala (poly-GA) aggregates resulting from aberrant translation of an expanded GGGGCC repeat in C9orf72, the most common genetic cause of amyotrophic lateral sclerosis and frontotemporal dementia. We find that poly-GA aggregates consist of densely packed twisted ribbons that recruit numerous 26S proteasome complexes, while other macromolecules are largely excluded. Proximity to poly-GA ribbons stabilizes a transient substrate-processing conformation of the 26S proteasome, suggesting stalled degradation. Thus, poly-GA aggregates may compromise neuronal proteostasis by driving the accumulation and functional impairment of a large fraction of cellular proteasomes.

INTRODUCTION

The ubiquitin-proteasome system (UPS) is the main cellular pathway for targeted protein degradation (Collins and Goldberg, 2017; Hershko et al., 2000). UPS alterations have been implicated in many human diseases, including multiple neurodegenerative disorders (Dantuma and Bott, 2014; Hipp et al., 2014; Schmidt and Finley, 2014). In particular, frontotemporal dementia (FTD) and amyotrophic lateral sclerosis (ALS) have been associated with mutations in UPS components (Deng et al., 2011; Johnson et al., 2010; Watts et al., 2004) and altered UPS

function (Cheroni et al., 2009; Tashiro et al., 2012). However, the contribution of UPS dysfunction to neurodegeneration and its underlying mechanisms are not yet well understood.

UPS impairment also has been linked to C9orf72 mutations, the most common genetic cause of ALS/FTD (Edbauer and Haass, 2016; Freibaum and Taylor, 2017; Gendron and Petrucci, 2017; Lin et al., 2017). A massive expansion of a GGGGCC (G₄C₂) repeat in a non-coding region of the C9orf72 gene to up to several thousand copies is found in 10%–50% of familial ALS/FTD cases and in 5%–7% of patients with sporadic disease (DeJesus-Hernandez et al., 2011; Majounie et al., 2012; Renton et al., 2011; van der Zee et al., 2013). Three non-mutually exclusive mechanisms have been suggested to mediate the toxicity of the G₄C₂ repeat expansion: (1) loss of native function of the C9orf72 protein due to reduced transcription of the mutant allele, (2) aberrant RNA interactions, and (3) production of toxic translation products and aggregates via repeat-associated non-ATG (RAN) translation (Zu et al., 2011).

Although the G₄C₂ repeat is found in a non-coding region of the C9orf72 gene, sense and anti-sense transcripts are unconventionally translated in all reading frames into five dipeptide-repeat proteins (Ash et al., 2013; Gendron et al., 2013; Mori et al., 2013a, 2013b; Zu et al., 2013): poly-GA, poly-GR, poly-GP, poly-PR, and poly-PA. While all five proteins form TDP-43-negative, p62-positive inclusions in ALS/FTD patient brain, the vast majority of these aggregates contain poly-GA (Mackenzie et al., 2015; Mori et al., 2013b; Zhang et al., 2014).

Poly-GA expression leads to toxicity in heterologous cells, primary neuron cultures, and mice (Jovićić et al., 2015; May et al., 2014; Schludi et al., 2017; Yamakawa et al., 2015; Zhang et al., 2014, 2016). Similar to other toxic aggregating proteins (Olzscha et al., 2011; Park et al., 2013), poly-GA aggregates sequester critical cellular factors including Unc119 and multiple UPS components (May et al., 2014; Zhang et al., 2016). UPS impairment is critically involved in poly-GA-mediated toxicity (Yamakawa et al., 2015; Zhang et al., 2014, 2016), but our



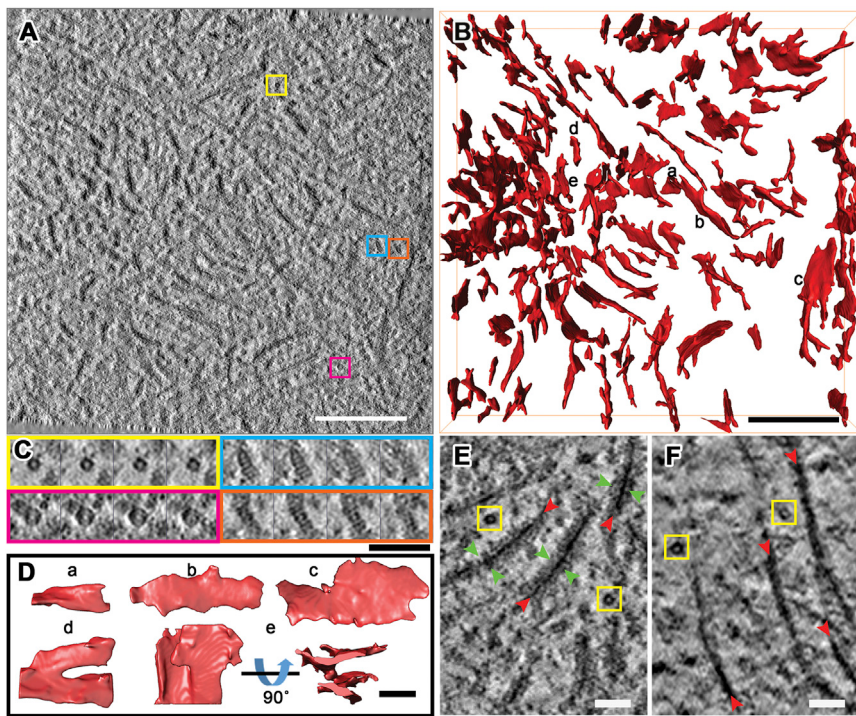


Figure 1. In Situ Neuronal Poly-GA Aggregates Form Twisted Ribbons

(A) Tomographic slice of an aggregate within a $(GA)_{175}$ -GFP-transduced neuron (DIV 5 + 5). Colored boxes show macromolecules magnified in (C).

(B) 3D rendering of the aggregate shown in (A). Selected poly-GA ribbons (red) magnified in (D) are indicated.

(C) Series of higher magnification tomographic slices of representative protein complexes detected in the tomogram shown in (A). Yellow and magenta boxes show the typical smaller (yellow) and larger (magenta) ring-like structures found in the aggregate region. Blue and orange boxes show side views of single-capped (blue) and double-capped (orange) 26S proteasomes.

(D) Selected ribbons from (B) rotated and magnified for visualization. Note the variable width of the ribbons (a-c). Some ribbons show bifurcations (d and e).

(E and F) Higher magnification tomographic slices of aggregates within neurons transduced with $(GA)_{175}$ -GFP (DIV 5 + 5) (E) or untagged $(GA)_{175}$ (DIV 5 + 5) (F). Yellow boxes mark similar small ring-like structures like in (A). Note that $(GA)_{175}$ -GFP ribbons (red arrowheads) are decorated by additional densities (green arrowheads), which are missing from untagged $(GA)_{175}$ ribbons. Tomographic slices are 5 nm thick.

Scale bars, 200 (A and B) and 50 nm (C-F).

See also Figure S1.

understanding of the underlying mechanisms remains incomplete. This is aggravated by the limited structural information currently available on poly-GA aggregates, especially within an unperturbed cellular context.

Here, we address these challenges using state-of-the-art cryo-electron tomography (cryo-ET) technologies, which allow 3D imaging of the cell interior in close-to-native conditions and at molecular resolution (Beck and Baumeister, 2016). We reveal the structure and cellular interactions of poly-GA aggregates within intact neurons to an unprecedented level of detail. Interestingly, we find that poly-GA aggregates consist of densely packed twisted ribbons that recruit large numbers of 26S proteasome complexes. Structural analysis of these proteasome complexes by subtomogram averaging and classification into functional states provides mechanistic insights into proteasomal dysfunction in *C9orf72* ALS/FTD.

RESULTS

Poly-GA Aggregates Contain Densely Packed Twisted Ribbons

To study neuronal poly-GA aggregates without interference from *C9orf72* loss-of-function and RNA-mediated toxicity, we transduced primary rat neuronal cultures with a GFP-tagged codon-modified synthetic construct expressing $(GA)_{175}$ -GFP using an ATG start codon (May et al., 2014). We have previously shown that lentiviral poly-GA expression results in inclusions of similar size and poly-GA intensity as in *C9orf72* patient tissue (May et al., 2014). Neurons were transduced at day *in vitro* (DIV) 5 and allowed to express the protein for another

5 days (DIV 5 + 5). The cultures were then vitrified and subsequently imaged by cryo-light microscopy to locate cellular poly-GA inclusions (Figure S1A). Correlative microscopy allowed the production of 100 to 200 nm-thick lamellas at the location of these aggregates using cryo-focused ion beam milling (Bauerlein et al., 2017; Rigort et al., 2012) (Figures S1B–S1D). Lastly, the samples were transferred to a cryo-transmission electron microscope for high-resolution 3D imaging by cryo-ET (Figures S1E and S1F).

Poly-GA aggregate cross-sections were typically $\sim 3 \mu\text{m}$ in diameter and consisted of a dense network of elongated polymorphic ribbons (Figures 1A and 1B). Whereas the thickness of the ribbons was well defined (13–15 nm), their length (100 nm–1 μm) and width (20–80 nm) varied considerably (Figure 1D, top). Our measurements likely underestimate ribbon length, as the parts of ribbons oriented perpendicular to the electron beam were not reliably detected because of missing information along this direction (Lucić et al., 2005). The ribbons were twisted along their axis with a variable helical pitch, and often bifurcated and/or associated laterally with neighboring ribbons (Figure 1D, bottom). This polymorphism contrasts with the uniform fibrils forming polyQ-expanded huntingtin exon 1 aggregates in mammalian cells (Bauerlein et al., 2017). Poly-GA ribbons were also more densely packed than polyQ fibrils, which occupied a lower fraction of the inclusion volume (poly-GA, $\geq 10\%$; polyQ, $\leq 4\%$). Thus, different amyloids adopt different morphologies *in situ*.

However, similarly to GFP-tagged polyQ fibrils, GFP-labeled poly-GA ribbons were decorated by additional densities (Figure 1E). To investigate the nature of these densities, neurons

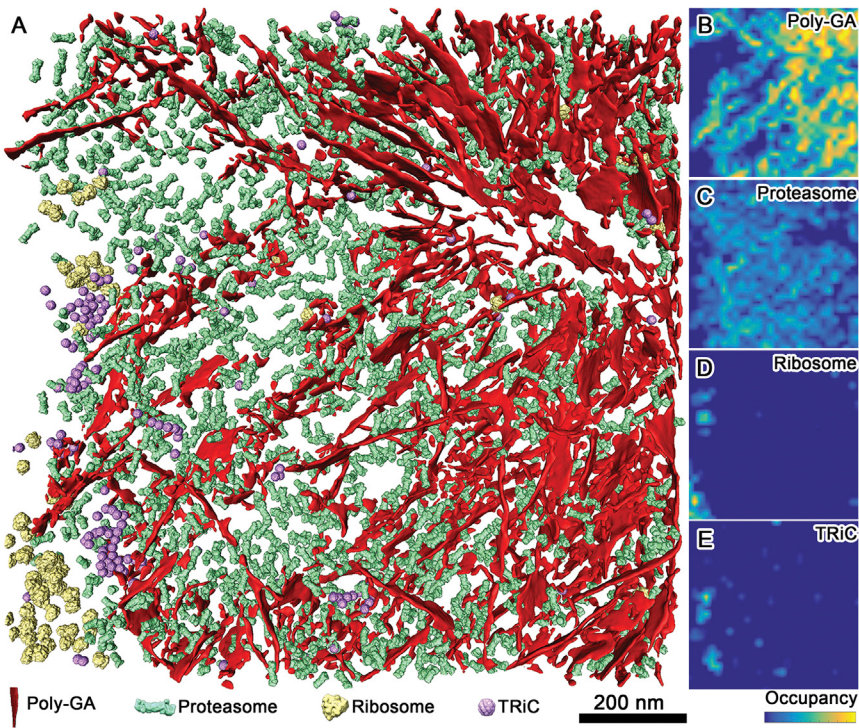


Figure 2. Mapping Macromolecules within Poly-GA Aggregates Shows a Substantial Recruitment of 26S Proteasomes

(A) 3D rendering of an aggregate within a neuron transduced with (GA)₁₇₅-GFP (DIV 5 + 5) showing different macromolecules found either within or at the periphery of the aggregate. Red, poly-GA ribbons; green, 26S proteasomes; yellow, ribosomes; purple, TRiC/CCT chaperonins. The macromolecules are mapped in their original locations and orientations, computationally determined by template matching and subtomogram averaging.

(B–E) Maximum intensity projection heatmaps of the molecular species shown in (A). Note that the proteasomes (C) are mostly found in between poly-GA ribbons (B), whereas ribosomes (D) almost exclusively occur outside of the aggregate. TRiC/CCT molecules (E) mostly populate the aggregate periphery, but some can also be found between poly-GA ribbons.

See also Figures S2–S5 and Movie S1.

sponding to the 26S proteasome (Chen et al., 2016a; Huang et al., 2016; Schweitzer et al., 2016; Wehner et al., 2017) for the smaller ring-like structures, and to the TRiC/CCT chaperonin (Leitner et al., 2012; Zang et al., 2016) for the larger ones (Figures 2, 3, and S3A–S3C; Movie S1). Other large UPS components, such as p97/VCP, did not appear abundant at poly-GA aggregates.

The abundance of TRiC/CCT complexes was not significantly different around poly-GA aggregates compared to the cell body of control neurons (untransduced or transduced with GFP only). However, the estimated concentration of proteasomes within the aggregate (~7 μM) was approximately 30-fold higher than in the cell body (Figure S4B) or the processes (Asano et al., 2015) of control cells. Given that poly-GA expression did not increase overall proteasome expression levels (Figure S4C), these data suggest that proteasomes are removed from other regions of the cell to accumulate within poly-GA aggregates. This is consistent with immunofluorescence staining (Figure S4A) and biochemical fractionation experiments showing reduced levels of Triton-soluble neuronal proteasomes (Figure S4C). Furthermore, our tomograms showed that 26S proteasomes almost exclusively accumulated within the aggregate interior (Figures 2 and S5A–S5D). Taken together, these results show that a substantial fraction of neuronal 26S proteasomes is sequestered into poly-GA aggregates.

To test the influence of the poly-GA expression level on proteasome recruitment, we analyzed aggregates formed in neurons at an earlier time point after transduction (DIV 5 + 3). Although these aggregates were smaller, they contained a similar concentration of proteasomes in their interior (Figure S5E). Importantly, analogous observations were made for poly-GA aggregates generated from a RAN-translated (G₄C₂)₇₃ construct, which more closely mimics the C9orf72 patient situation (Figures S4E and S5F). Thus, poly-GA aggregate morphology and proteasome recruitment were comparable in all the experimental conditions tested.

were co-transduced with untagged poly-GA and tagRFP-p62, as p62 co-localizes with poly-GA aggregates (May et al., 2014; Mori et al., 2013b; Yamakawa et al., 2015; Zhang et al., 2014) and allows targeting untagged poly-GA by correlative microscopy. As for polyQ fibrils (Bauerlein et al., 2017), the decorating densities were absent from untagged poly-GA ribbons (Figure 1F), demonstrating that these additional densities require GFP for their formation and that the ribbons consisted indeed of poly-GA aggregates. Thus, poly-GA forms amyloid-like ribbons in neurons.

26S Proteasomes Are Recruited to Poly-GA Aggregates

Unlike polyQ fibrils (Bauerlein et al., 2017), poly-GA ribbons did not visibly interact with cellular endomembranes. However, both the aggregate interior and periphery were densely populated by macromolecular complexes (Figures 1A, 1C, 1E, and 1F). Ribosomes were abundant around poly-GA aggregates but largely absent from their interior. In contrast, the space between poly-GA ribbons was densely populated with macromolecules that appeared as ~10-nm rings in tomographic cross-sections. Larger (~20 nm) cross-sectioned rings were also found at the aggregate periphery and occasionally in the interior. To investigate the identity of these macromolecules, we performed unbiased subtomogram averaging (Figure S2A). A small set of particles were hand-picked from the tomogram, aligned, and averaged. The resultant average was used as a template to computationally search the tomogram for additional occurrences of the same structure. These additional particles were then visually inspected, aligned, classified, and averaged again to produce a higher resolution average. The iterative application of this procedure yielded an average structure unequivocally corre-

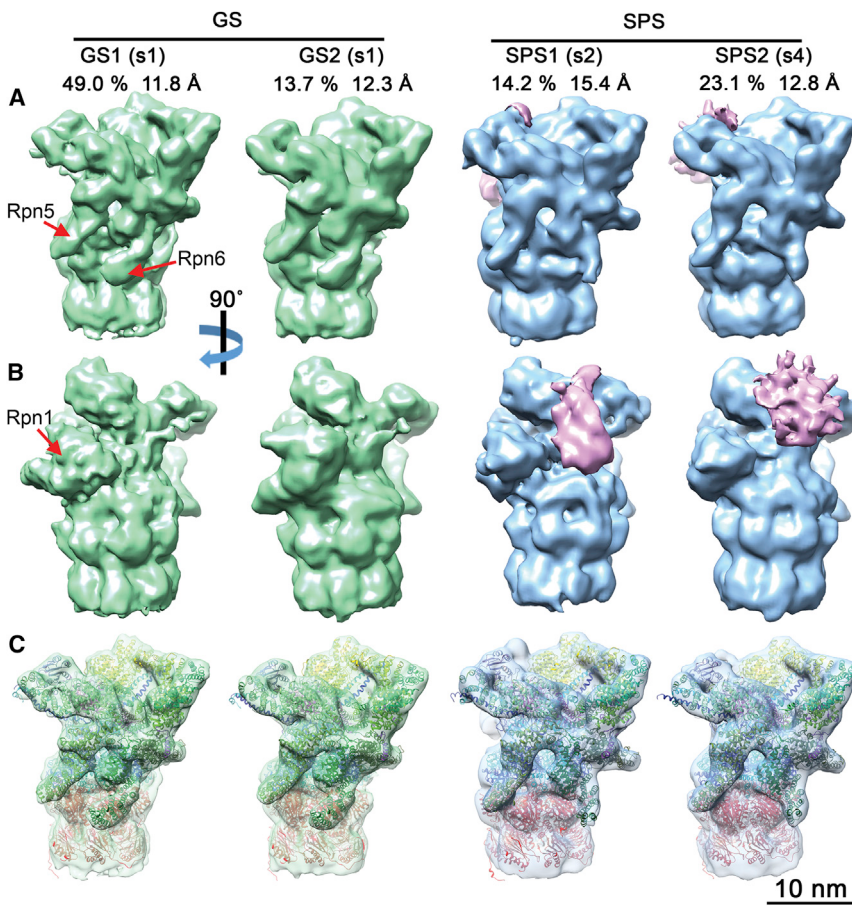


Figure 3. Subtomogram Classification of 26S Proteasomes Reveals Enrichment of Substrate Processing Conformations

(A–C) To analyze the functional state of proteasome regulatory particles, we cut single- and double-capped proteasomes by the half of the CP. The resultant half proteasomes were classified according to RP conformation into ground- or substrate-processing states (Asano et al., 2015), yielding two ground states (GS1, GS2) and two substrate-processing classes (SPS1, SPS2).

(A and B) The four density maps are displayed in solid surface representation in two different views. The positions of the Rpn1, Rpn5, and Rpn6 subunits are indicated. Prominent densities in the substrate binding region of SPS1 and SPS2 are colored in pink. For each class, the percentage of the total number of classified particles and the global resolution are indicated.

(C) Same view as (A), with semi-transparent maps superimposed with the atomic models generated by MDFF. The classes, respectively, represent the s1 state with different Rpn1 positions (GS1, GS2), the s2 state (SPS1), and the s4 state (SPS2). Atomic models are colored by subunits: Rpn1 (brown), Rpn2 (yellow), Rpn9/5/6/7/3/12 (different shades of green), Rpn8/Rpn11 (light/dark magenta), Rpn10 and Rpn13 (purple), AAA-ATPase hexamer (blue), and CP (red).

See also Figures S2 and S3 and Table S1.

interaction between the proteasome core and regulatory particles (Kleijnen et al., 2007) is apparently stabilized within poly-GA aggregates.

We further classified 26S proteasomes by RP conformation (Asano et al., 2015; Unverdorben et al., 2014). This yielded four well-defined classes, two of which (GS1, GS2) were consistent with the RP ground state conformation (s1), whereas the other two (SPS1, SPS2) corresponded to substrate processing states (s2–s4) (Figure 3). Interestingly, 37% of all 26S proteasomes belonged to substrate processing classes, almost twice the number than in control neurons (Asano et al., 2015) (Figures S3E and S3G). Thus, poly-GA aggregates recruit a large number of 26S proteasome regulatory particles, a substantial fraction of which adopts substrate processing conformations.

The relatively high resolution of the classes (11.8–15.4 Å) (Figures 3 and S3H) enabled us to assign each class to a functional state. To this end we employed molecular dynamics flexible fitting (MDFF) (Trabuco et al., 2009) initiated through the atomic models of the s1–s4 states of the yeast 26S proteasome (Figure 3C) (Wehmer et al., 2017). The s1 state was clearly the best fit for the GS1 and GS2 classes (Table S1). The yeast s1 structure fitted GS1 (49% of the total number of particles) without large discrepancies except for the position of the Rpn1 subunit, which in GS1 was similar to that observed in the human 26S proteasome (Chen et al., 2016a; Huang et al., 2016; Schweitzer et al., 2016). Also, in agreement with these studies, no prominent density was visible in our data for the Rpn13 subunit. The GS2 class (13.7% of particles) was overall similar to

Poly-GA Aggregation Alters Proteasome Structure

The 26S proteasome consists of a barrel-shaped 20S core particle (CP) that harbors the catalytic activity, bound to one or two 19S regulatory particles (RP). Regulatory particles are responsible for substrate recognition, unfolding, and translocation into the CP for proteolysis. Recent single-particle cryoelectron microscopy (cryo-EM) studies have revealed how RP conformational dynamics are coupled to the functional cycle of the 26S complex (Chen et al., 2016a; Unverdorben et al., 2014; Wehmer et al., 2017). Initial binding of substrates to the 26S proteasome presumably occurs in a low-energy ground state (s1) (see also Lu et al., 2015). Bound substrates are committed for degradation (s2 state) and then translocated into the CP (s3–s4 states). In the s4 state, the gate of the 20S CP is open, allowing the substrates to access the proteolytic chamber. We took advantage of the large number of proteasome complexes recruited to poly-GA aggregates to investigate their functional states *in situ* by subtomogram averaging and classification (Figure S2B).

We first sorted 26S proteasomes according to the number of regulatory particles (one or two) bound per CP. Previous structural (Asano et al., 2015) and biochemical (Tai et al., 2010) data indicated that in control neurons the large majority of 26S proteasomes contain only one RP (single-capped 26S). In striking contrast, 76% of poly-GA-associated 26S proteasomes were double-capped (Figures S3D and S3F). Therefore, the labile

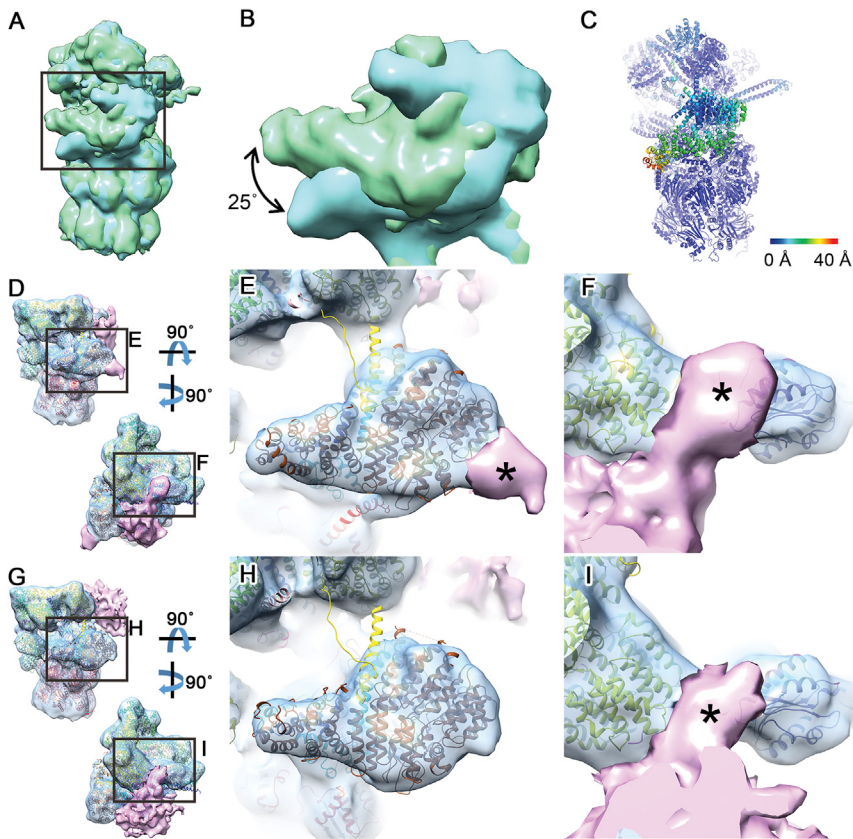


Figure 4. Detailed Structural Differences between 26S Proteasome Conformations Highlight Its *In Situ* Structural Dynamics and Interactions

(A) Superimposition of GS1 (green) and GS2 (cyan) density maps aligned by their CP. Both classes are consistent with the s1 state and differ only in the position of Rpn1.

(B) Magnified view of the region boxed in (A) showing a 25° rotation of the Rpn1 subunit in the GS2 map.

(C) Atomic model of the GS2 class colored according to the root-mean-square deviation (RMSD) from the GS1 model. Note that the only substantial differences are found in the Rpn1 region.

(D) Two views of the SPS1 map (consistent with the s2 state) shown in surface representation superimposed with its atomic model. A prominent density in the substrate binding region is colored in pink.

(E and F) Magnified view of the regions boxed in (D). The atomic models of Rpn1 (E), Rpn2, and Rpn10 (F) are shown in brown, yellow, and purple, respectively. Parts of the additional density denoted by asterisks may correspond to proteasome-bound ubiquitin or UBL domain proteins.

(G) Two views of the SPS2 map (consistent with the s4 state) shown in surface representation superimposed with its atomic model. A prominent density in the substrate binding region is colored in pink.

(H and I) Magnified view of the regions boxed in (G). Note that the density in the Rpn2/10 region is similar in the SPS1 and SPS2 class averages (I), whereas no additional density was found on the Rpn1 region of the SPS2 map (H).

GS1, but the Rpn1 subunit pivoted 25° on its N-terminal region to shift its C terminus toward the CP with respect to GS1 (Figures 4A–4C). This is a novel conformation of Rpn1, a particularly dynamic subunit (Asano et al., 2015; Huang et al., 2016; Schweitzer et al., 2016; Wehner et al., 2017) that serves as binding hub for 26S regulatory cofactors containing ubiquitin-like (UBL) domains (Elsasser et al., 2002; Leggett et al., 2002) and was recently identified as an ubiquitin receptor (Shi et al., 2016).

SPS1 proteasomes (14.2% of particles) were most similar to the substrate commitment state s2 (Table S1). In contrast, the SPS2 class (23.1% of particles) was best fitted by the s4 model of actively translocating proteasomes (Table S1). This is remarkable because, *in vitro*, the s4 state was only recently discovered in proteasomes incubated with non-hydrolyzable nucleotide analogs (Wehner et al., 2017), suggesting that it is normally a highly transient conformation. Thus, the interaction of poly-GA aggregates with the proteasome appears to stall its s4 conformation.

Both substrate processing classes showed prominent additional densities in the substrate binding region of the proteasome, in contact with the ATPase ring (Figure 3). In SPS1 the density was well defined (Figure 3), indicating a relatively stable interaction with the 26S complex that may in part correspond to bound UBL domain proteins (Aufderheide et al., 2015; Bashore et al., 2015). The density contacted Rpn1 (Figures 3, 4D, and 4E), consistent with the bound UBL domains of Rad23 or the ubiquitin C-terminal hydrolase 6 (Ubp6)/USP14 (Chen et al.,

2016b; Shi et al., 2016), and extended to another binding site of Rad23 at the Rpn10 subunit (Hiyama et al., 1999; Mueller and Feigon, 2003; Walters et al., 2002) (Figures 4D and 4F). Interestingly, similar to our SPS1 class, Ubp6-bound proteasomes have been shown to mainly adopt the s2 conformation (Aufderheide et al., 2015). Because the Rpn1 and Rpn10 UBL binding sites also interact with ubiquitin, proteasome-bound ubiquitinated substrates may also contribute to the extra density. Consistent with this notion, the estimated molecular mass of the density (~70 kDa) was larger than Ubp6 (56 kDa) or Rad23 (40/44 kDa for Rad23A/B). For the SPS2 class, the additional density contacted the Rpn10 subunit but not Rpn1 (Figures 4G–4I). The density was overall less well defined than for SPS1, indicating a more dynamic interaction, perhaps involving a more extensive participation of substrates (see below). Therefore, both substrates and cofactors may contribute to the additional densities found on substrate processing proteasomes.

Direct Interactions with Poly-GA Aggregates Impair Proteasome Function

To address the physiological role of the different proteasome conformations observed, we investigated their cellular distribution by mapping the particles back into the tomograms (Figure 5). We found that proteasome conformation correlated with the distance to poly-GA ribbons (Figures 5B–5E, $p < 0.001$, chi-square test, $n = 6,080$ regulatory particles from 4 tomograms).

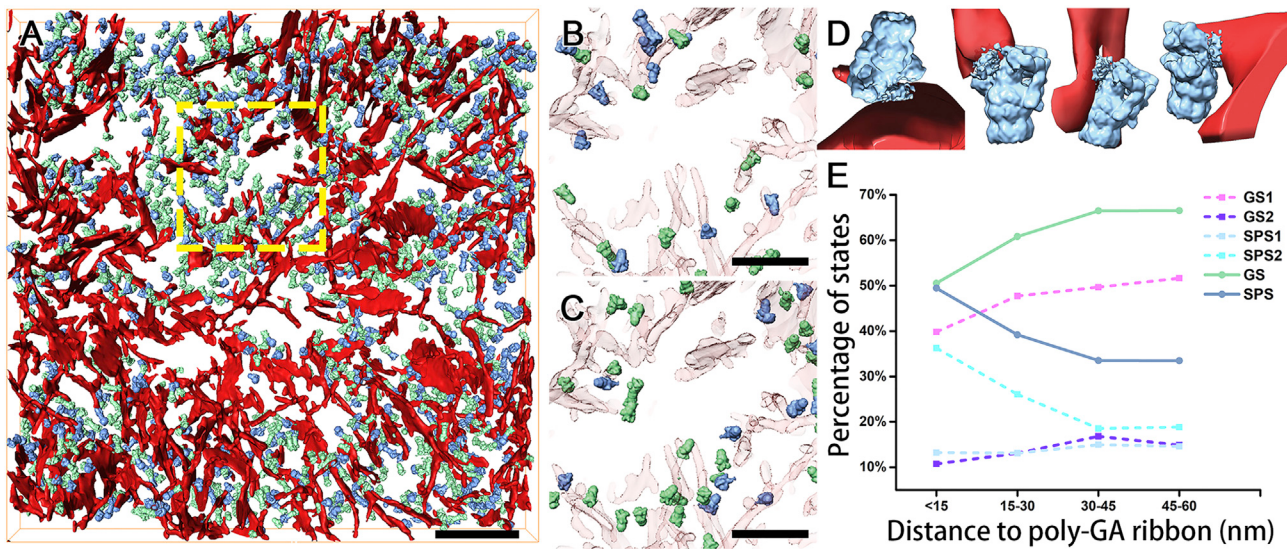


Figure 5. Spatial Mapping of Proteasomes within Poly-GA Aggregates Reveals Poly-GA Influence on Proteasome Conformation

(A) 3D rendering of an aggregate within a neuron transduced with $(GA)_{175}$ -GFP (DIV 5 + 5). Poly-GA ribbons (red), proteasomes in ground state (green), and proteasomes in substrate processing states (blue). Proteasome location and orientation were determined by template matching and subtomogram averaging. (B and C) Magnification of the region boxed in (A) showing only proteasomes less than 15 nm away from poly-GA ribbons (B) or 30–45 nm away (C). Poly-GA ribbons are shown as a transparent red surface. Note that substrate processing proteasomes are more abundant close to poly-GA ribbons.

(D) Examples of SPS2 proteasomes directly touching poly-GA ribbons in the tomogram shown in (A). The additional density in the substrate binding region overlaps with the poly-GA ribbons.

(E) Plot of proteasome conformation versus distance to poly-GA ribbons. The influence of the distance to poly-GA ribbons in proteasome conformation was statistically significant ($p < 0.001$, chi-square test, $n = 6,080$ regulatory particles from 4 tomograms).

Scale bars, 200 nm (A) and 100 nm (B and C).

See also Figure S4.

For proteasomes directly touching (Figure 5D) or very close to ribbons, the SPS2 class was overrepresented (36% versus 23% of the total proteasomes (Figure 5E), whereas the fraction of GS1 proteasomes was smaller than within the total (40% versus 49%) (Figure 5E). The fraction of GS1 proteasomes increased with their distance to ribbons, whereas SPS2 proteasomes followed the opposite trend. For SPS2 proteasomes associated with poly-GA ribbons, the contact interface was consistent with the location of the additional density observed in this class (Figures 3 and 4G–4I). Only small variations were found in the fractions of GS2 and SPS1 particles with respect to the distance to poly-GA ribbons (Figure 5E). These results indicate that association with poly-GA aggregates modifies the functional state of the 26S proteasome.

In agreement with this notion, functional measurements show that poly-GA expression impairs proteasome function (Figure S4D) (Yamakawa et al., 2015; Zhang et al., 2014). Interestingly, GA-rich sequences have been reported to slow or even stall proteasomal substrate processing in the context of the Epstein-Barr virus-encoded nuclear antigen 1 protein (Hoyt et al., 2006; Kraut, 2013; Levitskaya et al., 1997). Whereas *in vitro* the s4 state was only observed in the presence of non-hydrolysable nucleotide analogs (Wehmer et al., 2017), 23% of all proteasomes within neuronal poly-GA aggregates, and 36% of the proteasomes located in the immediate vicinity of poly-GA ribbons adopted the s4 conformation *in situ* (SPS2 class). Therefore, our results suggest that proteasomal degradation is slowed

down by poly-GA-mediated stalling of the otherwise highly transient s4 state. This may play an important role in the proteostasis impairment observed in poly-GA models.

DISCUSSION

Previous studies using classical EM reported that cellular poly-GA inclusions consist of a network of filaments 15–17 nm in diameter (Zhang et al., 2014, 2016). Our 3D imaging of unstained fully hydrated neurons shows that rather than filaments, poly-GA forms twisted ribbons similar to those observed *in vitro* for $(GA)_{15}$ (Chang et al., 2016). Whereas most amyloids are believed to be largely unbranched (Knowles et al., 2014), poly-GA ribbons bifurcated extensively. Together with their variable width, this suggests that *in situ* poly-GA ribbons are formed by different numbers of laterally stacked protofilaments. Furthermore, the similar morphology of $(GA)_{15}$ (Chang et al., 2016) and $(GA)_{175}$ (this study) ribbons is consistent with a molecular arrangement in which stacked GA-repeats give rise to the long axis of the protofilament.

Poly-GA aggregates recruited striking numbers of 26S proteasomes, whereas other macromolecules were excluded from the aggregate interior. This is remarkably different from our recent observations on polyQ inclusions, which interact with and may disrupt the membranes of the endoplasmic reticulum (ER) and other organelles, but do not harbor substantial numbers of 26S proteasomes or other large macromolecules (Bauerlein et al., 2017). This difference is surprising as proteasomes were also

reported to colocalize with polyQ aggregates (Bennett et al., 2005; Waelter et al., 2001). Thus, different aggregating proteins may trigger UPS dysfunction and cellular toxicity by distinct mechanisms, and how proteasomes associate with other disease-related aggregates remains to be elucidated (Deriziotis et al., 2011; Myeku et al., 2016). Future work should also address the extent of proteasome recruitment by aggregates of poly-GA proteins expressed at endogenous levels, as well as by other C9orf72 dipeptide-repeat proteins.

UPS impairment is known to play an important role in poly-GA induced toxicity (Yamakawa et al., 2015; Zhang et al., 2014, 2016). The proteasome and other UPS components are major poly-GA interactors in neurons (May et al., 2014), and poly-GA expression leads to reduced proteasome activity (Yamakawa et al., 2015; Zhang et al., 2014; our results). Our data provide mechanistic insights into these phenomena. First, poly-GA aggregates sequester a large fraction of cellular proteasomes, depleting them from other cellular functions critical for proteostasis maintenance, such as ER-associated degradation (Zhang et al., 2014). This may be particularly damaging to neurons given their extended morphology. Second, many of the poly-GA associated proteasomes may be functionally impaired. The fraction of double-capped proteasomes and proteasome RPs in substrate processing conformations was much higher within poly-GA aggregates than in control cells. Given that CP/RP interactions are stabilized during substrate degradation (Kleijnen et al., 2007), these data suggest that many poly-GA-associated proteasomes are processing substrates or stalled in the process. Consistently, our analysis shows that contact with poly-GA ribbons causes the proteasomes to adopt the s4 conformation, an otherwise highly transient intermediate state of substrate translocation (Wehmer et al., 2017). This is in line with previous reports that GA-rich sequences slow proteasomal translocation or even stall it (Kraut, 2013; Levitskaya et al., 1997). Interestingly, despite the strong association between proteasomes and poly-GA aggregates observed here, inhibiting proteasomal degradation does not affect poly-GA levels (Yamakawa et al., 2015). Therefore, the recruitment of proteasomes to poly-GA aggregates may be unproductive and may not lead to poly-GA degradation. The mechanisms driving such recruitment, which may involve ubiquitination of poly-GA and/or of associated factors, require further investigation.

Our data may also provide insights into the cellular mechanisms of proteasome regulation in the presence of protein aggregates. Poly-GA-associated proteasomes in substrate processing states showed additional densities that may correspond to bound ubiquitin and/or UBL domain-containing cofactors such as the deubiquitinating enzyme Ubp6/USP14 or the substrate shuttle factor Rad23 (Aufderheide et al., 2015; Bashore et al., 2015; Chen et al., 2016b; Shi et al., 2016). Although the binding of these factors to poly-GA-associated proteasomes remains to be conclusively demonstrated, several UBL domain proteins (Rad23, ubiquilin2, or Bag6) were highly enriched in the poly-GA interactome (May et al., 2014), and Rad23 is an important regulator of poly-GA induced toxicity (Zhang et al., 2016). UBL domain proteins strongly modulate proteasome activity (Finley et al., 2016) and have recently been implicated in neurodegeneration and aggregate clearance (Deng et al., 2011; Hjerpe et al.,

2016). Our results are consistent with the notion that UBL domain cofactors regulate the interactions of the proteasome with protein aggregates.

STAR★METHODS

Detailed methods are provided in the online version of this paper and include the following:

- KEY RESOURCES TABLE
- CONTACT FOR REAGENT AND RESOURCE SHARING
- EXPERIMENTAL MODEL AND SUBJECT DETAILS
 - Cell Culture
- METHOD DETAILS
 - Lentivirus Packaging
 - Generation of pcDNA3.1 – STOP-GA(G₄C₂)₇₃-GFP
 - Immunofluorescence and Cellular Fractionation
 - Flow Cytometry
 - Cryo-EM Sample Preparation
 - Cryo-Fluorescent Light Microscopy and Cryo-FIB Microscopy
 - Cryo-Electron Tomography and Reconstruction
 - Template Matching and Subtomogram Averaging
 - Atomic Model Fitting
 - Segmentation of Poly-GA Aggregates and Distance Measurement
- QUANTIFICATION AND STATISTICAL ANALYSES
- DATA AND SOFTWARE AVAILABILITY

SUPPLEMENTAL INFORMATION

Supplemental Information includes five figures, one table, and one movie and can be found with this article online at <https://doi.org/10.1016/j.cell.2017.12.030>.

ACKNOWLEDGMENTS

We thank Radostin Danev, Günter Pfeifer, Jürgen Plitzko, and Miroslava Schaffer for electron microscopy support, as well as Irina Dudanova and Eri Sakata for helpful discussions. The psPAX2 plasmid (Addgene plasmid # 12260) was a gift from Didier Trono. Q.G. is the recipient of postdoctoral fellowships from EMBO (EMBO ALTF 73-2015) and the Alexander von Humboldt Foundation. A.M.-S. is the recipient of a postdoctoral fellowship from the Séneca Foundation. This research has received funding from the European Commission (FP7 GA ERC-2012-SyG_318987-ToPAG and FP7 GA ERC-2013-CoG_617198 DPR-MODELS), the German Science Foundation (Excellence Cluster Center for Integrated Protein Science Munich [CIPSM]), Munich Cluster for Systems Neurology (SyNergy) (SFB-1035/Project A01), the NOMIS Foundation, the Helmholtz Association, and the NIH (Center for Macromolecular Modeling and Bioinformatics, grant 9P41GM104601).

AUTHOR CONTRIBUTIONS

Q.G. performed the electron microscopy experiments, computationally analyzed the data, and prepared the figures. C.L., H.H., and M.S.H. performed the cell culture and biochemistry experiments. A.M.-S. developed the software procedures for the data analysis. T.R. constructed the structural models. F.B. contributed to the computational analysis of the data. M.P.-B. and F.F. contributed the reagents. Q.G., M.S.H., F.-U.H., D.E., W.B., and R.F.-B. designed the research. D.E. and R.F.-B. supervised the experiments. Q.G., M.S.H., F.-U.H., D.E., W.B., and R.F.-B. wrote the manuscript.

DECLARATION OF INTERESTS

D.E. has a pending patent application on “Dipeptide-repeat proteins as therapeutic target in neurodegenerative diseases with hexanucleotide repeat expansion.”

Received: August 9, 2017

Revised: November 7, 2017

Accepted: December 20, 2017

Published: February 1, 2018

REFERENCES

- Asano, S., Fukuda, Y., Beck, F., Aufderheide, A., Förster, F., Danev, R., and Baumeister, W. (2015). Proteasomes. A molecular census of 26S proteasomes in intact neurons. *Science* 347, 439–442.
- Ash, P.E., Bieniek, K.F., Gendron, T.F., Caulfield, T., Lin, W.L., Dejesus-Hernandez, M., van Blitterswijk, M.M., Jansen-West, K., Paul, J.W., 3rd, Rademakers, R., et al. (2013). Unconventional translation of C9ORF72 GGGGCC expansion generates insoluble polypeptides specific to c9FTD/ALS. *Neuron* 77, 639–646.
- Aufderheide, A., Beck, F., Stengel, F., Hartwig, M., Schweitzer, A., Pfeifer, G., Goldberg, A.L., Sakata, E., Baumeister, W., and Förster, F. (2015). Structural characterization of the interaction of Ubp6 with the 26S proteasome. *Proc. Natl. Acad. Sci. USA* 112, 8626–8631.
- Bashore, C., Dambacher, C.M., Goodall, E.A., Matyskiela, M.E., Lander, G.C., and Martin, A. (2015). Ubp6 deubiquitinase controls conformational dynamics and substrate degradation of the 26S proteasome. *Nat. Struct. Mol. Biol.* 22, 712–719.
- Bauerlein, F.J.B., Saha, I., Mishra, A., Kalemanov, M., Martinez-Sanchez, A., Klein, R., Dusanova, I., Hipp, M.S., Hartl, F.U., Baumeister, W., et al. (2017). In situ architecture and cellular interactions of polyQ inclusions. *Cell* 171, 179–187.e10.
- Beck, M., and Baumeister, W. (2016). Cryo-electron tomography: can it reveal the molecular sociology of cells in atomic detail? *Trends Cell Biol.* 26, 825–837.
- Bennett, E.J., Bence, N.F., Jayakumar, R., and Kopito, R.R. (2005). Global impairment of the ubiquitin-proteasome system by nuclear or cytoplasmic protein aggregates precedes inclusion body formation. *Mol. Cell* 17, 351–365.
- Bharat, T.A., and Scheres, S.H. (2016). Resolving macromolecular structures from electron cryo-tomography data using subtomogram averaging in RELION. *Nat. Protoc.* 11, 2054–2065.
- Chang, Y.J., Jeng, U.S., Chiang, Y.L., Hwang, I.S., and Chen, Y.R. (2016). The glycine-alanine dipeptide repeat from C9orf72 hexanucleotide expansions forms toxic amyloids possessing cell-to-cell transmission properties. *J. Biol. Chem.* 291, 4903–4911.
- Chen, S., Wu, J., Lu, Y., Ma, Y.B., Lee, B.H., Yu, Z., Ouyang, Q., Finley, D.J., Kirschner, M.W., and Mao, Y. (2016a). Structural basis for dynamic regulation of the human 26S proteasome. *Proc. Natl. Acad. Sci. USA* 113, 12991–12996.
- Chen, X., Randles, L., Shi, K., Tarasov, S.G., Aihara, H., and Walters, K.J. (2016b). Structures of Rpn1 T1:Rad23 and hRpn13:hPLIC2 reveal distinct binding mechanisms between substrate receptors and shuttle factors of the proteasome. *Structure* 24, 1257–1270.
- Cheroni, C., Marino, M., Tortarolo, M., Veglianese, P., De Biasi, S., Fontana, E., Zuccarello, L.V., Maynard, C.J., Dantuma, N.P., and Bendotti, C. (2009). Functional alterations of the ubiquitin-proteasome system in motor neurons of a mouse model of familial amyotrophic lateral sclerosis. *Hum. Mol. Genet.* 18, 82–96.
- Collins, G.A., and Goldberg, A.L. (2017). The logic of the 26S proteasome. *Cell* 169, 792–806.
- Dantuma, N.P., and Bott, L.C. (2014). The ubiquitin-proteasome system in neurodegenerative diseases: precipitating factor, yet part of the solution. *Front. Mol. Neurosci.* 7, 70.
- Dantuma, N.P., Lindsten, K., Glas, R., Jellne, M., and Masucci, M.G. (2000). Short-lived green fluorescent proteins for quantifying ubiquitin/proteasome-dependent proteolysis in living cells. *Nat. Biotechnol.* 18, 538–543.
- De Smet, F., Saiz Rubio, M., Hompes, D., Naus, E., De Baets, G., Langenberg, T., Hipp, M.S., Houben, B., Claes, F., Charbonneau, S., et al. (2017). Nuclear inclusion bodies of mutant and wild-type p53 in cancer: a hallmark of p53 inactivation and proteostasis remodelling by p53 aggregation. *J. Pathol.* 242, 24–38.
- DeJesus-Hernandez, M., Mackenzie, I.R., Boeve, B.F., Boxer, A.L., Baker, M., Rutherford, N.J., Nicholson, A.M., Finch, N.A., Flynn, H., Adamson, J., et al. (2011). Expanded GGGGCC hexanucleotide repeat in noncoding region of C9ORF72 causes chromosome 9p-linked FTD and ALS. *Neuron* 72, 245–256.
- Deng, H.X., Chen, W., Hong, S.T., Boycott, K.M., Gorrie, G.H., Siddique, N., Yang, Y., Fecto, F., Shi, Y., Zhai, H., et al. (2011). Mutations in UBQLN2 cause dominant X-linked juvenile and adult-onset ALS and ALS/dementia. *Nature* 477, 211–215.
- Deriziotis, P., André, R., Smith, D.M., Goold, R., Kinghorn, K.J., Kristiansen, M., Nathan, J.A., Rosenzweig, R., Kruta, D., Glickman, M.H., et al. (2011). Misfolded PrP impairs the UPS by interaction with the 20S proteasome and inhibition of substrate entry. *EMBO J.* 30, 3065–3077.
- Edbauer, D., and Haass, C. (2016). An amyloid-like cascade hypothesis for C9orf72 ALS/FTD. *Curr. Opin. Neurobiol.* 36, 99–106.
- Elsasser, S., Gali, R.R., Schwickart, M., Larsen, C.N., Leggett, D.S., Müller, B., Feng, M.T., Tübing, F., Dittmar, G.A., and Finley, D. (2002). Proteasome subunit Rpn1 binds ubiquitin-like protein domains. *Nat. Cell Biol.* 4, 725–730.
- Fernandez, J.J., Laugks, U., Schaffer, M., Bäuerlein, F.J., Khoshouei, M., Baumeister, W., and Lucic, V. (2016). Removing contamination-induced reconstruction artifacts from cryo-electron tomograms. *Biophys. J.* 110, 850–859.
- Finley, D., Chen, X., and Walters, K.J. (2016). Gates, channels, and switches: Elements of the [proteasome machine. *Trends Biochem. Sci.* 41, 77–93.
- Freibaum, B.D., and Taylor, J.P. (2017). The role of dipeptide repeats in C9ORF72-related ALS-FTD. *Front. Mol. Neurosci.* 10, 35.
- Gendron, T.F., and Petrucelli, L. (2017). Disease mechanisms of C9ORF72 repeat expansions. *Cold Spring Harb. Perspect. Med.*, a024224.
- Gendron, T.F., Bieniek, K.F., Zhang, Y.J., Jansen-West, K., Ash, P.E., Caulfield, T., Daugherty, L., Dunmore, J.H., Castaneda-Casey, M., Chew, J., et al. (2013). Antisense transcripts of the expanded C9ORF72 hexanucleotide repeat form nuclear RNA foci and undergo repeat-associated non-ATG translation in c9FTD/ALS. *Acta Neuropathol.* 126, 829–844.
- Goh, B.C., Hadden, J.A., Bernardi, R.C., Singharoy, A., McGreevy, R., Rudack, T., Cassidy, C.K., and Schulten, K. (2016). Computational methodologies for real-space structural refinement of large macromolecular complexes. *Annu. Rev. Biophys.* 45, 253–278.
- Hershko, A., Ciechanover, A., and Varshavsky, A. (2000). Basic medical research award. The ubiquitin system. *Nat. Med.* 6, 1073–1081.
- Hipp, M.S., Bersuker, K., and Kopito, R.R. (2012a). Live-cell imaging of ubiquitin-proteasome system function. *Methods Mol. Biol.* 832, 463–472.
- Hipp, M.S., Patel, C.N., Bersuker, K., Riley, B.E., Kaiser, S.E., Shaler, T.A., Brandeis, M., and Kopito, R.R. (2012b). Indirect inhibition of 26S proteasome activity in a cellular model of Huntington’s disease. *J. Cell Biol.* 196, 573–587.
- Hipp, M.S., Park, S.H., and Hartl, F.U. (2014). Proteostasis impairment in protein-misfolding and -aggregation diseases. *Trends Cell Biol.* 24, 506–514.
- Hiyama, H., Yokoi, M., Masutani, C., Sugawara, K., Maekawa, T., Tanaka, K., Hoeijmakers, J.H., and Hanaoka, F. (1999). Interaction of hHR23 with S5a. The ubiquitin-like domain of hHR23 mediates interaction with S5a subunit of 26S proteasome. *J. Biol. Chem.* 274, 28019–28025.
- Hjerpe, R., Bett, J.S., Keuss, M.J., Solovyova, A., McWilliams, T.G., Johnson, C., Sahu, I., Varghese, J., Wood, N., Wightman, M., et al. (2016). UBQLN2 mediates autophagy-independent protein aggregate clearance by the proteasome. *Cell* 166, 935–949.
- Hoyt, M.A., Zich, J., Takeuchi, J., Zhang, M., Govaerts, C., and Coffino, P. (2006). Glycine-alanine repeats impair proper substrate unfolding by the proteasome. *EMBO J.* 25, 1720–1729.

- Hrabe, T., Chen, Y., Pfeffer, S., Cuellar, L.K., Mangold, A.V., and Förster, F. (2012). PyTom: a python-based toolbox for localization of macromolecules in cryo-electron tomograms and subtomogram analysis. *J. Struct. Biol.* 178, 177–188.
- Huang, X., Luan, B., Wu, J., and Shi, Y. (2016). An atomic structure of the human 26S proteasome. *Nat. Struct. Mol. Biol.* 23, 778–785.
- Humphrey, W., Dalke, A., and Schulten, K. (1996). VMD: visual molecular dynamics. *J. Mol. Graph.* 14, 33–38, 27–38.
- Johnson, J.O., Mandrioli, J., Benatar, M., Abramzon, Y., Van Deerlin, V.M., Trojanowski, J.Q., Gibbs, J.R., Brunetti, M., Gronka, S., Wu, J., et al.; ITALSGEN Consortium (2010). Exome sequencing reveals VCP mutations as a cause of familial ALS. *Neuron* 68, 857–864.
- Jovičić, A., Mertens, J., Boeynaems, S., Bogaert, E., Chai, N., Yamada, S.B., Paul, J.W., 3rd, Sun, S., Herdy, J.R., Bieri, G., et al. (2015). Modifiers of C9orf72 dipeptide repeat toxicity connect nucleocytoplasmic transport defects to FTD/ALS. *Nat. Neurosci.* 18, 1226–1229.
- Khatter, H., Myasnikov, A.G., Natchiar, S.K., and Klaholz, B.P. (2015). Structure of the human 80S ribosome. *Nature* 520, 640–645.
- Kleijnen, M.F., Roelofs, J., Park, S., Hathaway, N.A., Glickman, M., King, R.W., and Finley, D. (2007). Stability of the proteasome can be regulated allosterically through engagement of its proteolytic active sites. *Nat. Struct. Mol. Biol.* 14, 1180–1188.
- Knowles, T.P., Vendruscolo, M., and Dobson, C.M. (2014). The amyloid state and its association with protein misfolding diseases. *Nat. Rev. Mol. Cell Biol.* 15, 384–396.
- Kraut, D.A. (2013). Slippery substrates impair ATP-dependent protease function by slowing unfolding. *J. Biol. Chem.* 288, 34729–34735.
- Kremer, J.R., Mastronarde, D.N., and McIntosh, J.R. (1996). Computer visualization of three-dimensional image data using IMOD. *J. Struct. Biol.* 116, 71–76.
- Kuhn, P.H., Wang, H., Dislich, B., Colombo, A., Zeitschel, U., Ellwart, J.W., Kremmer, E., Rossner, S., and Lichtenhaller, S.F. (2010). ADAM10 is the physiologically relevant, constitutive alpha-secretase of the amyloid precursor protein in primary neurons. *EMBO J.* 29, 3020–3032.
- Lee, Y.B., Chen, H.J., Peres, J.N., Gomez-Deza, J., Attig, J., Stalekar, M., Troakes, C., Nishimura, A.L., Scotter, E.L., Vance, C., et al. (2013). Hexanucleotide repeats in ALS/FTD form length-dependent RNA foci, sequester RNA binding proteins, and are neurotoxic. *Cell Rep.* 5, 1178–1186.
- Leggett, D.S., Hanna, J., Borodovsky, A., Crosas, B., Schmidt, M., Baker, R.T., Walz, T., Ploegh, H., and Finley, D. (2002). Multiple associated proteins regulate proteasome structure and function. *Mol. Cell* 10, 495–507.
- Leitner, A., Joachimiak, L.A., Bracher, A., Mönkemeyer, L., Walzthoeni, T., Chen, B., Pechmann, S., Holmes, S., Cong, Y., Ma, B., et al. (2012). The molecular architecture of the eukaryotic chaperonin TRiC/CCT. *Structure* 20, 814–825.
- Levitskaya, J., Sharipo, A., Leonchik, A., Ciechanover, A., and Masucci, M.G. (1997). Inhibition of ubiquitin/proteasome-dependent protein degradation by the Gly-Ala repeat domain of the Epstein-Barr virus nuclear antigen 1. *Proc. Natl. Acad. Sci. USA* 94, 12616–12621.
- Li, X., Mooney, P., Zheng, S., Booth, C.R., Braunfeld, M.B., Gubbens, S., Agard, D.A., and Cheng, Y. (2013). Electron counting and beam-induced motion correction enable near-atomic-resolution single-particle cryo-EM. *Nat. Methods* 10, 584–590.
- Lin, G., Mao, D., and Bellen, H.J. (2017). Amyotrophic lateral sclerosis pathogenesis converges on defects in protein homeostasis associated with TDP-43 mislocalization and proteasome-mediated degradation overload. *Curr. Top. Dev. Biol.* 121, 111–171.
- Lu, Y., Lee, B.H., King, R.W., Finley, D., and Kirschner, M.W. (2015). Substrate degradation by the proteasome: a single-molecule kinetic analysis. *Science* 348, 1250834.
- Lucić, V., Yang, T., Schweikert, G., Förster, F., and Baumeister, W. (2005). Morphological characterization of molecular complexes present in the synaptic cleft. *Structure* 13, 423–434.
- Mackenzie, I.R., Arzberger, T., Kremmer, E., Troost, D., Lorenzl, S., Mori, K., Weng, S.M., Haass, C., Kretzschmar, H.A., Edbauer, D., and Neumann, M. (2013). Dipeptide repeat protein pathology in C9ORF72 mutation cases: clinico-pathological correlations. *Acta Neuropathol.* 126, 859–879.
- Mackenzie, I.R., Frick, P., Grässer, F.A., Gendron, T.F., Petrucelli, L., Cashman, N.R., Edbauer, D., Kremmer, E., Prudlo, J., Troost, D., and Neumann, M. (2015). Quantitative analysis and clinico-pathological correlations of different dipeptide repeat protein pathologies in C9ORF72 mutation carriers. *Acta Neuropathol.* 130, 845–861.
- Majounie, E., Renton, A.E., Mok, K., Dopper, E.G., Waite, A., Rollinson, S., Chiò, A., Restagno, G., Nicolaou, N., Simon-Sánchez, J., et al.; Chromosome 9-ALS/FTD Consortium; French research network on FTLD/FTLD/ALS; ITALSGEN Consortium (2012). Frequency of the C9orf72 hexanucleotide repeat expansion in patients with amyotrophic lateral sclerosis and frontotemporal dementia: a cross-sectional study. *Lancet Neurol.* 11, 323–330.
- Martinez-Sánchez, A., García, I., Asano, S., Lucic, V., and Fernandez, J.J. (2014). Robust membrane detection based on tensor voting for electron tomography. *J. Struct. Biol.* 186, 49–61.
- Mastronarde, D.N. (2005). Automated electron microscope tomography using robust prediction of specimen movements. *J. Struct. Biol.* 152, 36–51.
- May, S., Hornburg, D., Schludi, M.H., Arzberger, T., Rentzsch, K., Schwenk, B.M., Grässer, F.A., Mori, K., Kremmer, E., Banzhaf-Strathmann, J., et al. (2014). C9orf72 FTLD/ALS-associated Gly-Ala dipeptide repeat proteins cause neuronal toxicity and Unc119 sequestration. *Acta Neuropathol.* 128, 485–503.
- Mori, K., Arzberger, T., Grässer, F.A., Gijselinck, I., May, S., Rentzsch, K., Weng, S.M., Schludi, M.H., van der Zee, J., Cruts, M., et al. (2013a). Bidirectional transcripts of the expanded C9orf72 hexanucleotide repeat are translated into aggregating dipeptide repeat proteins. *Acta Neuropathol.* 126, 881–893.
- Mori, K., Weng, S.M., Arzberger, T., May, S., Rentzsch, K., Kremmer, E., Schmid, B., Kretzschmar, H.A., Cruts, M., Van Broeckhoven, C., et al. (2013b). The C9orf72 GGGGCC repeat is translated into aggregating dipeptide-repeat proteins in FTLD/ALS. *Science* 339, 1335–1338.
- Mueller, T.D., and Feigon, J. (2003). Structural determinants for the binding of ubiquitin-like domains to the proteasome. *EMBO J.* 22, 4634–4645.
- Myeku, N., Clelland, C.L., Emrani, S., Kukushkin, N.V., Yu, W.H., Goldberg, A.L., and Duff, K.E. (2016). Tau-driven 26S proteasome impairment and cognitive dysfunction can be prevented early in disease by activating cAMP-PKA signaling. *Nat. Med.* 22, 46–53.
- Nickell, S., Förster, F., Linaroudis, A., Net, W.D., Beck, F., Hegerl, R., Baumeister, W., and Plitzko, J.M. (2005). TOM software toolbox: acquisition and analysis for electron tomography. *J. Struct. Biol.* 149, 227–234.
- Olzscha, H., Schermann, S.M., Woerner, A.C., Pinkert, S., Hecht, M.H., Tartaglia, G.G., Vendruscolo, M., Hayer-Hartl, M., Hartl, F.U., and Vabulas, R.M. (2011). Amyloid-like aggregates sequester numerous metastable proteins with essential cellular functions. *Cell* 144, 67–78.
- Park, S.H., Kukushkin, Y., Gupta, R., Chen, T., Konagai, A., Hipp, M.S., Hayer-Hartl, M., and Hartl, F.U. (2013). PolyQ proteins interfere with nuclear degradation of cytosolic proteins by sequestering the Sis1p chaperone. *Cell* 154, 134–145.
- Pettersen, E.F., Goddard, T.D., Huang, C.C., Couch, G.S., Greenblatt, D.M., Meng, E.C., and Ferrin, T.E. (2004). UCSF Chimera—a visualization system for exploratory research and analysis. *J. Comput. Chem.* 25, 1605–1612.
- Phillips, J.C., Braun, R., Wang, W., Gumbart, J., Tajkhorshid, E., Villa, E., Chipot, C., Skeel, R.D., Kalé, L., and Schulten, K. (2005). Scalable molecular dynamics with NAMD. *J. Comput. Chem.* 26, 1781–1802.
- Renton, A.E., Majounie, E., Waite, A., Simón-Sánchez, J., Rollinson, S., Gibbs, J.R., Schymick, J.C., Laaksovirta, H., van Swieten, J.C., Mallykangas, L., et al.; ITALSGEN Consortium (2011). A hexanucleotide repeat expansion in C9ORF72 is the cause of chromosome 9p21-linked ALS-FTD. *Neuron* 72, 257–268.
- Ribeiro, J.V., Bernardi, R.C., Rudack, T., Stone, J.E., Phillips, J.C., Freddolino, P.L., and Schulten, K. (2016). QwikMD—Integrative molecular dynamics toolkit for novices and experts. *Sci. Rep.* 6, 26536.

- Rigort, A., Bäuerlein, F.J., Villa, E., Eibauer, M., Laugks, T., Baumeister, W., and Plitzko, J.M. (2012). Focused ion beam micromachining of eukaryotic cells for cryoelectron tomography. *Proc. Natl. Acad. Sci. USA* **109**, 4449–4454.
- Scheres, S.H., and Chen, S. (2012). Prevention of overfitting in cryo-EM structure determination. *Nat. Methods* **9**, 853–854.
- Schindelin, J., Arganda-Carreras, I., Frise, E., Kaynig, V., Longair, M., Pietzsch, T., Preibisch, S., Rueden, C., Saalfeld, S., Schmid, B., et al. (2012). Fiji: an open-source platform for biological-image analysis. *Nat. Methods* **9**, 676–682.
- Schludi, M.H., Becker, L., Garrett, L., Gendron, T.F., Zhou, Q., Schreiber, F., Popper, B., Dimou, L., Strom, T.M., Winkelmann, J., et al. (2017). Spinal poly-GA inclusions in a C9orf72 mouse model trigger motor deficits and inflammation without neuron loss. *Acta Neuropathol.* **134**, 241–254.
- Schmidt, M., and Finley, D. (2014). Regulation of proteasome activity in health and disease. *Biochim. Biophys. Acta* **1843**, 13–25.
- Schroeder, W., Martin, K.M., and Lorensen, W.E. (2006). The Visualization Toolkit: an object-oriented approach to 3D graphics (Kitware).
- Schweitzer, A., Aufderheide, A., Rudack, T., Beck, F., Pfeifer, G., Plitzko, J.M., Sakata, E., Schulten, K., Förster, F., and Baumeister, W. (2016). Structure of the human 26S proteasome at a resolution of 3.9 Å. *Proc. Natl. Acad. Sci. USA* **113**, 7816–7821.
- Shi, Y., Chen, X., Elsasser, S., Stocks, B.B., Tian, G., Lee, B.H., Shi, Y., Zhang, N., de Poot, S.A., Tuebing, F., et al. (2016). Rpn1 provides adjacent receptor sites for substrate binding and deubiquitination by the proteasome. *Science* **351**, pii: aad9421.
- Tai, H.C., Besche, H., Goldberg, A.L., and Schuman, E.M. (2010). Characterization of the brain 26S proteasome and its interacting proteins. *Front. Mol. Neurosci.* **3**, 12.
- Tashiro, Y., Urushitani, M., Inoue, H., Koike, M., Uchiyama, Y., Komatsu, M., Tanaka, K., Yamazaki, M., Abe, M., Misawa, H., et al. (2012). Motor neuron-specific disruption of proteasomes, but not autophagy, replicates amyotrophic lateral sclerosis. *J. Biol. Chem.* **287**, 42984–42994.
- Tivol, W.F., Briegel, A., and Jensen, G.J. (2008). An improved cryogen for plunge freezing. *Microsc. Microanal.* **14**, 375–379.
- Trabuco, L.G., Villa, E., Schreiner, E., Harrison, C.B., and Schulten, K. (2009). Molecular dynamics flexible fitting: a practical guide to combine cryo-electron microscopy and X-ray crystallography. *Methods* **49**, 174–180.
- Unverdorben, P., Beck, F., Śledź, P., Schweitzer, A., Pfeifer, G., Plitzko, J.M., Baumeister, W., and Förster, F. (2014). Deep classification of a large cryo-EM dataset defines the conformational landscape of the 26S proteasome. *Proc. Natl. Acad. Sci. USA* **111**, 5544–5549.
- van der Zee, J., Gijsselinck, I., Dillen, L., Van Langenhove, T., Theuns, J., Engelborghs, S., Philtjens, S., Vandenbulcke, M., Sleegers, K., Sieben, A., et al.; European Early-Onset Dementia Consortium (2013). A pan-European study of the C9orf72 repeat associated with FTLD: geographic prevalence, genomic instability, and intermediate repeats. *Hum. Mutat.* **34**, 363–373.
- Waelter, S., Boeddrich, A., Lurz, R., Scherzinger, E., Lueder, G., Lehrach, H., and Wanker, E.E. (2001). Accumulation of mutant huntingtin fragments in aggresome-like inclusion bodies as a result of insufficient protein degradation. *Mol. Biol. Cell* **12**, 1393–1407.
- Walters, K.J., Kleijnen, M.F., Goh, A.M., Wagner, G., and Howley, P.M. (2002). Structural studies of the interaction between ubiquitin family proteins and proteasome subunit S5a. *Biochemistry* **41**, 1767–1777.
- Watts, G.D., Wymer, J., Kovach, M.J., Mehta, S.G., Mumm, S., Darvish, D., Pestronk, A., Whyte, M.P., and Kimonis, V.E. (2004). Inclusion body myopathy associated with Paget disease of bone and frontotemporal dementia is caused by mutant valosin-containing protein. *Nat. Genet.* **36**, 377–381.
- Wehmer, M., Rudack, T., Beck, F., Aufderheide, A., Pfeifer, G., Plitzko, J.M., Förster, F., Schulten, K., Baumeister, W., and Sakata, E. (2017). Structural insights into the functional cycle of the ATPase module of the 26S proteasome. *Proc. Natl. Acad. Sci. USA* **114**, 1305–1310.
- Yamakawa, M., Ito, D., Honda, T., Kubo, K., Noda, M., Nakajima, K., and Suzuki, N. (2015). Characterization of the dipeptide repeat protein in the molecular pathogenesis of c9FTD/ALS. *Hum. Mol. Genet.* **24**, 1630–1645.
- Zang, Y., Jin, M., Wang, H., Cui, Z., Kong, L., Liu, C., and Cong, Y. (2016). Staggered ATP binding mechanism of eukaryotic chaperonin TRiC (CCT) revealed through high-resolution cryo-EM. *Nat. Struct. Mol. Biol.* **23**, 1083–1091.
- Zhang, Y.J., Jansen-West, K., Xu, Y.F., Gendron, T.F., Bieniek, K.F., Lin, W.L., Sasaguri, H., Caulfield, T., Hubbard, J., Daugherty, L., et al. (2014). Aggregation-prone c9FTD/ALS poly(GA) RAN-translated proteins cause neurotoxicity by inducing ER stress. *Acta Neuropathol.* **128**, 505–524.
- Zhang, Y.J., Jansen-West, K., Xu, Y.F., Grima, J.C., Sasaguri, H., Jansen-West, K., Xu, Y.F., Katzman, R.B., Gass, J., Murray, M.E., Shinohara, M., et al. (2016). C9ORF72 poly(GA) aggregates sequester and impair HR23 and nucleocytoplasmic transport proteins. *Nat. Neurosci.* **19**, 668–677.
- Zu, T., Gibbons, B., Doty, N.S., Gomes-Pereira, M., Huguet, A., Stone, M.D., Margolis, J., Peterson, M., Markowski, T.W., Ingram, M.A., et al. (2011). Non-ATG-initiated translation directed by microsatellite expansions. *Proc. Natl. Acad. Sci. USA* **108**, 260–265.
- Zu, T., Liu, Y., Bañez-Coronel, M., Reid, T., Pletnikova, O., Lewis, J., Miller, T.M., Harms, M.B., Falchook, A.E., Subramony, S.H., et al. (2013). RAN proteins and RNA foci from antisense transcripts in C9ORF72 ALS and frontotemporal dementia. *Proc. Natl. Acad. Sci. USA* **110**, E4968–E4977.

STAR★METHODS

KEY RESOURCES TABLE

REAGENT or RESOURCE	SOURCE	IDENTIFIER
Antibodies		
Rabbit polyclonal anti-PSMC4	Bethyl Laboratories	Cat# A303-850A; RRID: AB_2620201
Goat anti rabbit Alexa 555	Thermo Fisher Scientific	Cat# A-21429; RRID: AB_2535850
Goat anti mouse Alexa 555	Thermo Fisher Scientific	Cat# A-21424; RRID: AB_141780
Goat anti rabbit Alexa 647	Thermo Fisher Scientific	Cat# A-21245; RRID: AB_2535813
Mouse monoclonal GFP	NeuroMab	Cat# 75-131; RRID: AB_10671445
Mouse monoclonal anti-GA	Mackenzie et al., 2013	N/A
Rabbit polyclonal anti-Calnexin	Enzo Life Sciences	Cat# ADI-SPA-860; RRID: AB_10616095
Chemicals, Peptides, and Recombinant Proteins		
4x Laemmli buffer	Biorad	Cat# 1610747
B27	Thermo Fisher Scientific	Cat# 17504044
Borax anhydrous	Sigma	Cat# 71996
Bovine serum albumin	Sigma	Cat# BQ3716
DMEM, high glucose, GlutaMAX	Thermo Fisher Scientific	Cat# 10566-016
DNase	Sigma	Cat# DN25
Fetal calf serum	Sigma-Aldrich	Cat# F7524
Gelatin	Sigma-Aldrich	Cat# G9391
HEPES	Biomol	Cat# 05288
L-Glutamine	Thermo Fisher Scientific	Cat# 25030081
Lipofectamine 2000	Thermo Fisher Scientific	Cat# 11668-019
MEM non-essential amino acids solution	Thermo Fisher Scientific	Cat# 11140050
MgCl ₂	Merck	Cat# 105833
NaCl	Merck	Cat# 106404
Na ₂ HPO ₄ * 2 H ₂ O	Merck	Cat# 106580
Neurobasal medium	Thermo Fisher Scientific	Cat# 21103049
Opti-MEM reduced serum medium	Thermo Fisher Scientific	Cat# 31985070
Paraformaldehyde	Sigma-Aldrich	Cat# 76240
Penicillin-streptomycin	Thermo Fisher Scientific	Cat# 15140122
Poly-D-lysine	Sigma	Cat# P1149
Protease inhibitor cocktail	Sigma	Cat# P8340
Sucrose	Sigma Aldrich	Cat# S9378
Tricine gels	Thermo Fisher Scientific	Cat# EC66252BOX
Dulbecco's modified Eagle medium (DMEM)	Biochrom	Cat# F0435
Fetal bovine serum	GIBCO	Cat# 10270-106
L-Glutamine	GIBCO	Cat# 25030-024
Non-essential amino acids	GIBCO	Cat# 11140-035
Trypsin	GIBCO	Cat# 12605-010
PBS	GIBCO	Cat# 20012-068
FuGENE 6	Promega	Cat# E2691
Deposited Data		
Cryo-EM model of the <i>S. cerevisiae</i> 26S proteasome (s1 state)	Wehmer et al., 2017	PDB: 5MP9, 5MPD
Cryo-EM model of the <i>S. cerevisiae</i> 26S proteasome (s2 state)	Wehmer et al., 2017	PDB: 5MPA, 5MPE
Cryo-EM model of the <i>S. cerevisiae</i> 26S proteasome (s3 state)	Wehmer et al., 2017	PDB: 5MPB
Cryo-EM model of the <i>S. cerevisiae</i> 26S proteasome (s4 state)	Wehmer et al., 2017	PDB: 5MPC

(Continued on next page)

Continued

REAGENT or RESOURCE	SOURCE	IDENTIFIER
Hybrid model of the <i>S. cerevisiae</i> TRiC/CCT	Leitner et al., 2012	PDB: 4V94
Cryo-EM map of the human 80S ribosome	Khatter et al., 2015	EMDB: 2938
<i>In situ</i> subtomogram average of the GS1 conformation of the 26S proteasome from rat neurons	This paper	EMDB: EMD-3916
Fitted model of the GS1 conformation of the 26S proteasome from rat neurons	This paper	PDB: 6EPF
<i>In situ</i> subtomogram average of the GS2 conformation of the 26S proteasome from rat neurons	This paper	EMDB: EMD-3913
Fitted model of the GS2 conformation of the 26S proteasome from rat neurons	This paper	PDB: 6EPC
<i>In situ</i> subtomogram average of the SPS1 conformation of the 26S proteasome from rat neurons	This paper	EMDB: EMD-3914
Fitted model of the SPS1 conformation of the 26S proteasome from rat neurons	This paper	PDB: 6EPD
<i>In situ</i> subtomogram average of the SPS2 conformation of the 26S proteasome from rat neurons	This paper	EMDB: EMD-3915
Fitted model of the SPS2 conformation of the 26S proteasome from rat neurons	This paper	PDB: 6EPE
<i>In situ</i> subtomogram average of TRiC from rat neurons	This paper	EMDB: EMD-3917
<i>In situ</i> cryo-electron tomogram of C9ORF72 poly-GA aggregates within a rat neuron	This paper	EMDB: EMD-4191
Experimental Models: Cell Lines		
HEK293FT	Thermo Fisher Scientific	Cat# R70007
UbG76V-GFP HEK293 stable cell line	De Smet et al., 2017	N/A
Experimental Models: Organisms/Strains		
Primary neuronal cultures from CD (SD) IGS rats	Charles River	CD-SIFA; RRID: RGD_734476
Recombinant DNA		
Plasmid: FhSynW-GFP	May et al., 2014	N/A
Plasmid: FhSynW-175xGA-GFP	May et al., 2014	N/A
Plasmid: FU3a-tagRFP-T2 human p62	This paper	N/A
Plasmid: FhSynW -GA149stop	This paper	N/A
Plasmid: pcDNA3.1-VSVG	Kuhn et al., 2010	N/A
Plasmid: psPAX2	Gift from Didier Trono (unpublished data)	Addgene Cat# 12260
Plasmid: pcDNA3.1-STOP-GA(G ₄ C ₂) ₇₃ -GFP	This paper	N/A
Software and Algorithms		
SerialEM	Mastronarde, 2005	http://bio3d.colorado.edu/SerialEM/
TomSegMemTV	Martinez-Sanchez et al., 2014	https://sites.google.com/site/3demimageprocessing/tomosegmemtv
MaskTomRec	Fernandez et al., 2016	https://sites.google.com/site/3demimageprocessing/masktomrec
K2Align	Dimitry Tegunov	https://github.com/dtegunov/k2align
Pytom	Hrabe et al., 2012	http://pytom.org/
RELION	Bharat and Scheres, 2016	http://www.mrc-lmb.cam.ac.uk/relion/index.php/Main_Page
UCSF CHIMERA	Pettersen et al., 2004	http://www.cgl.ucsf.edu/chimera
OriginPro	OriginLab	https://www.originlab.com/index.aspx?go=Products/Origin
MATLAB	MathWorks	https://www.mathworks.com/
IMOD	Kremer et al., 1996	http://bio3d.colorado.edu/imod/

(Continued on next page)

Continued

REAGENT or RESOURCE	SOURCE	IDENTIFIER
VTK	N/A	https://www.vtk.org ; RRID: SCR_015013
Python scripts used to measure the distance between proteasomes and poly-GA aggregates	This paper	https://github.com/anmartinez/poly-GA
QwikMD	Ribeiro et al., 2016	http://www.ks.uiuc.edu/Research/qwikmd/
VMD	Humphrey et al., 1996	http://www.ks.uiuc.edu/Research/vmd/
NAMD	Phillips et al., 2005	http://www.ks.uiuc.edu/Research/namd/
TOM toolbox	Nickell et al., 2005	https://www.biochem.mpg.de/tom
Amira	Thermo Fisher Scientific	https://www.fei.com/software/amira-3d-for-life-sciences/ ; RRID: SCR_014305
Other		
Quantifoil grids 200 mesh Gold R2/1	Quantifoil Micro Tools	N/A
Whatman filter paper #1	Whatman	Cat# 1001090
Nunc 12 well plates	Thermo Fisher	Cat# 150628
Glass coverslips	VWR	Cat# 631-1581

CONTACT FOR REAGENT AND RESOURCE SHARING

Further information and requests for resources and reagents should be directed to and will be fulfilled by the Lead Contact, Wolfgang Baumeister (baumeiste@biochem.mpg.de).

EXPERIMENTAL MODEL AND SUBJECT DETAILS**Cell Culture**

HEK293 cells (female) stably expressing UbG76V-GFP ([Dantuma et al., 2000](#); [De Smet et al., 2017](#)) were cultured in Dulbecco's modified Eagle's medium (DMEM; Biochrom) supplemented with 10% (v/v) fetal bovine serum (GIBCO), 2 mM L-glutamine (GIBCO), penicillin-streptomycin (Thermo Fisher) and non-essential amino acids (GIBCO). Transfection was carried out using FuGENE 6 (Promega).

Rats (IGS background, Charles River; RRID:RGD_734476) were housed in a pathogen-free facility with 12:12 h light/dark cycle and food/water available *ad libitum*. All animal experiments were performed in compliance with institutional policies approved by the government of Upper Bavaria following §11 Ab.1 TierSchG for the DZNE animal facility (Inst.-Nr. 04-26). Primary cortical neurons were prepared from embryonic day 19 animals of both sexes. Neocortex and hippocampus were dissected in ice-cold dissection media (HBBS, penicillin-streptomycin, 10 mM HEPES pH 7.3). The tissue was enzymatically dissociated at 37°C (for cortices 20 min in 0.2% trypsin, 0.7 mg/ml DNase I; for hippocampi 15 min in 0.25% trypsin in dissection media) followed by gentle trituration.

For EM analysis, 250,000 cells/ml cortical neurons were plated on EM grids and cultured in Neurobasal medium containing 2% B27 (Thermo Fisher), penicillin-streptomycin, 0.5 mM L-glutamine (Thermo Fisher). For biochemical analysis, 250,000 cells/ml cortical neurons were plated on 12-well plates (Thermo Fisher) and cultured in Neurobasal medium. For immunofluorescence experiments, 85,000 cells/ml hippocampal neurons were plated on 12-well plates containing glass coverslips (VWR) coated with poly-D-lysine and cultured in Neurobasal medium supplemented with 12.5 µM glutamate.

METHOD DETAILS**Lentivirus Packaging**

HEK293FT cells (female; from Thermo Fisher) of low passage number were plated in three 10 cm dishes (5,000,000 cells/dish) and cultured in DMEM (Thermo Fisher), penicillin-streptomycin, 1% non-essential amino acids (Thermo Fisher) and 10% fetal bovine serum (Sigma). A transfection mix was set up as follows: 18.6 µg transfer vector (FhSynW-(GA)₁₇₅-GFP, FhSynW (GA)₁₄₉, FU3a-tagRFP-p62 or FhSynW-GFP), 11 µg pSPAX2 and 6.4 µg pVSvg in 4.5 mL Opti-MEM were combined with 108 µl Lipofectamine 2000 in 4.5 mL Opti-MEM (Thermo Fisher) and incubated for 20 minutes. Cell media was replaced with 5 mL Opti-MEM and 3 mL of transfection mix were added per dish. The transfection media was replaced after 6 h by plating media supplemented with 13 mg/ml bovine serum albumin, and the supernatant was collected after additional 24 h. Lentiviral particles were harvested by ultracentrifugation using a Sw28 rotor (22,000 rpm, 2 h), resuspended in 150 µl Neurobasal media on a rocking platform overnight and stored in aliquots at -80°C.

Generation of pcDNA3.1 – STOP-GA(G₄C₂)₇₃-GFP

The method to generate the construct was adapted from [Lee et al. \(2013\)](#). Complementary G₄C₂ repeat oligonucleotides with phosphorylated ends (5'-PHOS-(G₄C₂)₅-3' and 5'-PHOS-CC(G₂C₄)₄GGCC-3') were energetically optimized to maximize heterodimer formation. After initial denaturation for 5 min at 95°C in T4 ligase buffer (New England Biolabs), the complementary oligonucleotides were allowed to anneal by slow cool down to room temperature during 2 h. Hybridized oligonucleotides were then self-ligated for 1 h to extend the G₄C₂ DNA sequence. Adaptor oligonucleotides containing NheI (5') and BamHI (3') restriction sites (5' adaptor oligonucleotides containing NheI: 5'-GCCGTCAAGGCCGCATCTAGTAGCTAGC-3' and 5'-PHOS-CCGCTAGCTACTAGATGCGGCCTT GACGGC-3'; 3' adaptor oligonucleotides containing BamHI: 5'-PHOS-GGGATCCCTAGTACTGGGCCTCATGGC-3' and 5'-GCC CATGAGGCCAGTACTAGGGATC-3') were separately hybridized and sequentially added in excess to the ligation reaction mix to stop G₄C₂ elongation. Ligation products were separated in a 1.25% agarose gel, and bands running at the desired molecular size were excised. The DNA was then purified with the Zymoclean Gel DNA recovery kit (Zymo Research) according to the manufacturer's guidelines. The resulting blunt-end fragments were phosphorylated and cloned into a dephosphorylated SmaI-restricted pUC18 plasmid for amplification. Colonies were screened for G₄C₂ repeat length, and a construct with 73 G₄C₂ repeats was chosen for further experiments. The selected sequence was subcloned into the mammalian expression vector pcDNA3.1(+)myc-His between NheI and BamHI in front of a GFP-encoding region. Finally, multiple stop codons were added by site-directed mutagenesis in every reading frame at the 5' of the sequence of interest, thereby removing all initiator codons between the T7 promoter and the sequence of interest. The sequence was verified by multiple sequencing reactions as well as restriction digest.

Immunofluorescence and Cellular Fractionation

Immunofluorescence stainings were performed on primary hippocampal neurons 5 days after infection with (GA)₁₇₅-GFP or GFP lentivirus on day 5, or 3 days upon transfection with G₄C₂ on day 3 using Lipofectamine 2000 (Thermo Fisher). Cells were fixed for 10 min at room temperature (4% paraformaldehyde, 4% sucrose in PBS). Anti-PSMC4 (Bethyl Laboratories, 1:250, RRID:AB_2620201) or anti-GA ([Mackenzie et al., 2013](#), 1:200) primary antibodies as well as secondary antibodies (Alexa 555, Alexa 647, Thermo Fisher, 1:400, RRID:AB_2535850, RRID:AB_141780, RRID:AB_2535813) were diluted in staining buffer (0.1% gelatin, 0.3% Triton X-100, 450 mM NaCl, 16 mM sodium phosphate pH 7.4). After mounting the coverslips, images were taken using a LSM710 confocal microscope (Carl Zeiss, Jena) with a 63 × oil immersion objective.

Biochemical experiments were performed on primary cortical neurons 10 days after infection with either (GA)₁₇₅-GFP or GFP lentivirus on day 3. Cells were lysed (PBS with 1% Triton X-100, 15 mM MgCl₂, 0.2 mg/ml DNase with protease inhibitor cocktail). Upon centrifugation (18,000 xg, 4°C for 30 min) the soluble fraction was collected from the supernatant. The pellets were washed twice with lysis buffer yielding the insoluble fraction. After adding 4x Laemmli buffer (Bio-Rad), samples were denatured (95°C for 10 min) and loaded on Tricine gradient gels (Thermo Fisher). The following antibodies were used: Anti-PSMC4 (Bethyl Laboratories, 1:1000), anti-GFP (NeuroMab, 1:5000, RRID:AB_10671445) and anti-Calnexin (Enzo Life Sciences, 1:7000, RRID:AB_10616095). The data in [Figure S4C](#) was normalized to the total proteasome levels in GFP-transduced control neurons.

Flow Cytometry

HEK293 cells stably expressing UbG76V-GFP were harvested 72 h after transient transfection with (GA)₁₇₅-tagRFP or tagRFP as control and analyzed with a BD FACSAriaII flow cytometer, as described previously ([Hipp et al., 2012a, 2012b](#)). In brief, to ensure a sufficient number of cells with elevated levels of the transfected proteins > 100,000 events were analyzed per condition. To plot the level of the reporter protein versus the level of the transfected protein, a set of gates was established in the tagRFP channel. HEK293 cells transfected with tagRFP were used as single-color control to compensate the bleed-through between GFP and tag-RFP individually for each gate, and to correct for effects due to high expression of tagRFP. The compensated mean fluorescence of the reporter protein UbG76V-GFP in each of these gates was plotted on the y axis and the gate number (corresponding to the log of fluorescence intensity of the transfected protein) was plotted on the x axis. The data shown in [Figure S4D](#) are from a single representative experiment out of three independent repeats. Cells expressing low levels of tagRFP (gates 1-9) and gates with < 1000 events were not included in the analysis. Raw flow cytometry data were analyzed using FlowJo software (version 9.9; Tree Star).

Cryo-EM Sample Preparation

Quantifoil grids (R2/1, Au 200 mesh grid, Quantifoil Micro Tools, Germany) were coated with an additional carbon layer (~20 nm thick) using a carbon evaporator (MED 020, BAL-TEC). Before use, the grids were glow discharged using a plasma cleaner (PDC-3XG, Harrick) for 20 s and neurons were seeded as described above. Neurons were vitrified 5 days after transduction with GFP or tagRFP-p62/untagged (GA)₁₇₅ on day 5, 3 or 5 days after transduction with (GA)₁₇₅-GFP on day 5, and 3 days after transfection with (G₄C₂)₇₃ on day 3. Untransduced and untransfected control neurons were vitrified on DIV 10.

For vitrification, the grids were blotted for 10 s from the back side using filter paper and immediately plunged into a liquid ethane/propane mixture ([Tivol et al., 2008](#)) using a manual plunge freezer. Grids were transferred to sealed boxes and stored in liquid nitrogen until usage.

Cryo-Fluorescent Light Microscopy and Cryo-FIB Microscopy

EM grids were mounted onto modified Autogrid (FEI, Hillsboro, OR, USA) sample carriers, allowing subsequent FIB milling with a shallow incident ion beam (Rigort et al., 2012), and then transferred to the cryo-stage of an FEI CorrSight microscope for cryo-light microscopy. Overview images of the grid and poly-GA-GFP/tagRFP-p62 signal were respectively acquired in transmitted light and the spinning disk confocal modes using a 20x lens (air, N.A. 0.8). Image acquisition was done with FEI MAPS software. The samples were then transferred into a FEI Scios dual beam cryo-FIB/scanning electron microscope (SEM) using a cryo-transfer system.

To improve the sample conductivity, a layer of organometallic platinum was deposited onto the grid using the *in situ* gas injection system with the following parameters: 10 mm working distance, 26°C pre-heating temperature, and 8 s gas injection time. MAPS software allowed correlation between cryo-light microscopy and SEM images via the 3-point alignment method. Thin lamellas were prepared in the regions of poly-GA-GFP/tagRFP-p62 fluorescence signal using the Ga²⁺ ion beam at 30 kV under a 20° stage tilt angle. 0.5 nA beam current was used for rough milling, followed by sequentially lower currents during the thinning procedure. A current of 30 pA was used for the final polishing step to reach a final lamella thickness of 150–200 nm. SEM imaging was used to monitor the milling progress.

Cryo-Electron Tomography and Reconstruction

The specimens were examined at liquid nitrogen temperature in an FEI Titan Krios cryo-electron microscope operated at 300 kV and equipped with a field emission gun and a Gatan post column energy filter. Lamellas were loaded vertical to the tilt axis, and were precisely aligned by adjusting the β angle of the cryo-stage. Images were collected using a 4 k × 4 k K2 Summit (Gatan) direct detector camera operated in dose fractionation mode (0.4 s, 0.3 electrons/Å² per frame). Tilt series were recorded using SerialEM software (Mastronarde, 2005) at a nominal magnification of 42,000 X, resulting in a pixel size of 3.42 Å at the specimen level. Unidirectional tomographic tilt series were recorded from –50° to +70° with an increment of 2°. On average, 6 frames were collected for each image resulting in a total dose between 100 e[−]/Å² to 110 e[−]/Å² per tilt series. K2 frames were aligned using in house software (K2Align) based on previous work (Li et al., 2013). Tilt series were aligned using fiducial-less patch tracking, and the tomograms were reconstructed by weighted back projection using the IMOD software package (Kremer et al., 1996). For tomograms of lamellas superficially contaminated by ice crystals, a surface cleaning procedure was employed after alignment (Fernandez et al., 2016). The resulting tilt series were then aligned and reconstructed again to obtain the final reconstructions.

Template Matching and Subtomogram Averaging

To identify the macromolecules found in the tomograms, a *de novo* subtomogram averaging procedure without any external structural information was developed (Figure S2A). The MATLAB (Mathworks) TOM toolbox (Nickell et al., 2005) was used as general platform for image processing. First, all the tomograms were binned twice (13.68 Å³ per voxel) for processing. In one tomogram, several identical small ring-like structures were hand-picked, aligned and averaged to obtain a first tube-like average structure. This was used as an initial template for template matching in all the binned tomograms using PyTom (Hrabe et al., 2012). The resulting subtomograms were cropped, CTF-corrected and classified using Relion (Bharat and Scheres, 2016). The resulting structure clearly showed a 20S proteasome core complex, but because of the missing wedge and the preferred orientation induced by the initial template, the 19S regulatory particles (RP) were not well resolved. This structure was used to perform a new round of template matching and classification, which clearly resolved proteasomes either single- or doubled-capped. The single-capped proteasome were low-pass filtered to 40 Å and used as a reference for template matching again to produce the final dataset. In total, 10,367 proteasome subtomograms of 180³ pixel volume were picked for further analysis from 9 tomograms containing large (GA)₁₇₅-GFP aggregates (DIV 5 + 5). The same template matching procedure was applied to tomograms of control neurons, either untransduced (16 tomograms) or transduced with GFP only (17 tomograms).

The subtomograms were then 3D classified using Relion (Figure S2B). They were first divided into single-capped and double-capped proteasomes. To further rule out reference bias, a single-capped proteasome, a double-capped proteasome and a mirrored single-capped proteasome were used as references for classification. The results were similar, indicating negligible reference bias during classification. To further analyze the conformational status of the 19S regulatory particles, all subtomograms were cut *in silico* between the β-rings of the 20S, resulting in two independent particles for the double-capped proteasomes (Asano et al., 2015). All cut-out half proteasomes were merged into a new dataset for another round of classification. Ground state and substrate processing state structures were distinguished by the relative orientation of the Rpn5 and Rpn6 subunits (Asano et al., 2015; Unverdorben et al., 2014). Ground state and substrate processing state structures were further classified by applying a soft sphere mask in the RP region only. Identical subclasses were merged resulting in two ground state and two substrate processing state classes, which were further refined to achieve the final structures. A similar analysis could not be applied to control neurons (GFP-transduced or untransduced) due to the low numbers of proteasomes found in these samples. Therefore, the results from untransduced neurons from a previous study (Asano et al., 2015) were used as reference. Visualization of the subtomogram averages was performed in UCSF Chimera (Pettersen et al., 2004). Resolution was determined using the 0.143 criterion according to the gold standard Fourier Shell Correlation (Scheres and Chen, 2012).

To identify the larger ring-like structures found in the tomograms, a similar template matching procedure was employed. A spherical structure was generated after processing, which showed a clear eight-fold symmetry by rotational correlation coefficient analysis (Figure S3B). Furthermore, the size of the average fitted well with the crystal structure of TRiC/CCT (PDB: 4V94) (Leitner et al., 2012),

indicating that these larger rings correspond to the TRiC/CCT chaperonin. A total of 1,366 TRiC subtomograms were used for averaging. For ribosome template matching, a human 80S ribosome structure (EMDB 2938) (Khatter et al., 2015) was filtered to 40 Å and used as a template.

Atomic Model Fitting

The *S. cerevisiae* proteasome models of the states s1 (PDB: 5MP9, 5MPD), s2 (PDB: 5MPA, 5MPE), s3 (PDB: 5MPB), and s4 (PDB: 5MPC) (Wehmer et al., 2017) were used as initial models. The core particles of the models were fitted into each of the groups obtained by classification of the poly-GA proteasome dataset using rigid body docking within UCSF Chimera. For each class, MDFF was performed to refine the s1-4 models according to the density maps. Then, the RMSD between the best fitting atomic models and the initial s1-4 state models was calculated (Table S1). This showed that the GS1 class reflected the s1 state with the Rpn1 positioning of the human s1 state (PDB: 5L5K) (Schweitzer et al., 2016), GS2 reflected the s1 state with a rotated Rpn1 position, SPS1 reflected the s2 state and SPS2 reflected the s4 state. To obtain the final atomic rat models, the best fitting yeast structures for each class were used as templates for comparative modeling and real-space structure refinement (Goh et al., 2016). MDFF simulations were prepared using QwikMD (Ribeiro et al., 2016), analyzed with VMD (Humphrey et al., 1996), and carried out with NAMD (Phillips et al., 2005).

Segmentation of Poly-GA Aggregates and Distance Measurement

Poly-GA ribbons are locally planar and were consequently segmented using a filter based on tensor voting, which distinguishes planar-like from line- and blob-like structures (Martinez-Sanchez et al., 2014). The filter outputs a scalar map, where voxel intensity value is proportional to the local similarity with a plane. The final segmentation was generated by thresholding the filter output combined with a manually generated mask to discard other locally planar structures like membranes and correct minor artifacts. Due to the missing information along the electron beam direction (Lucić et al., 2005), poly-GA ribbons were not clearly visible when oriented within the xy plane. Segmentations were visualized using Amira (Thermo Fischer, RRID:SCR_014305).

For Figure 5, proteasome regulatory particles and poly-GA ribbons were represented by an isosurface, properly placed and oriented in their original tomogram. For regulatory particles, surfaces were obtained by applying the marching cubes algorithm, implemented in the VTK Open Source library (<https://www.vtk.org/>; RRID:SCR_015013; Schroeder et al., 2006), on the corresponding subtomogram average. Isosurface threshold was set manually for every case with the criterion of choosing the minimum value avoiding noisy features. For poly-GA ribbons, isosurfaces were generated from the output of the planar filter using the marching cubes algorithm. The final ribbon surfaces were obtained by masking the isosurface with the corresponding ribbon segmentation from the tomogram. To calculate the fraction of the volume of poly-GA inclusions occupied by poly-GA ribbons, total ribbon volume was measured from the segmentations and divided by the total tomogram volume. For this calculation, tomograms (n = 4, (GA)₁₇₅-GFP transduced neurons at DIV 5 + 5) were selected in which the large majority of the volume contained poly-GA aggregates.

RP to poly-GA ribbon distance was defined as the shortest Euclidean distance between the center of the RP to any surface point of any ribbon in the same tomogram. A custom Python software package was developed to measure RP-to-ribbon distance for every RP in all tomograms. The results were grouped by particle class to facilitate statistical analysis. The shortest distance among surfaces was computed with the help of a VTK library (Schroeder et al., 2006).

QUANTIFICATION AND STATISTICAL ANALYSES

To measure proteasome concentration, for each tomogram (n = 9, (GA)₁₇₅-GFP transduced neurons, DIV 5 + 5; n = 17, GFP transduced neurons; n = 16, untransduced neurons) the number of proteasomes found by template matching and subtomogram averaging was divided by the total tomogram volume. Because other cellular structures (such as poly-GA aggregates, other macromolecules or cellular organelles) were also present in the tomogram volume, this calculation underestimates the cytosolic concentration of proteasomes. For poly-GA aggregates, only tomograms with more than half volume occupied by aggregates were considered for the concentration calculation. In Figure S4B, the top and bottom boundaries of the boxes indicate $\pm 2\sigma$ standard error, and whiskers extend to the maximum and minimum values. Statistical analysis was performed by the non-parametric Mann-Whitney test, as not all data was normally distributed according to the Shapiro-Wilk test.

For the analysis of proteasome conformation as a function of the distance to poly-GA ribbons (Figures 5B, 5C, and 5E), 6080 regulatory particles from 4 tomograms of (GA)₁₇₅-GFP transduced neurons (DIV 5 + 5) were analyzed. The data were divided in a 4x4 Table (4 RP states x 4 distance bins) resulting in 9 degrees of freedom. Statistical analysis was performed by Chi-square test.

The proteasome levels in the total, soluble and insoluble fractions of (GA)₁₇₅-GFP transduced neurons were quantified from western blots by measuring the gray levels using Fiji (Schindelin et al., 2012). Error bars in Figure S4C indicate standard error. All data was normally distributed according to the Shapiro-Wilk test (95% confidence level). Statistical analysis was performed by two-sided paired t test (n = 6 replicates from 4 independent experiments). All graphs were plotted using OriginPro (OriginLab).

DATA AND SOFTWARE AVAILABILITY

The Python scripts used to calculate the distance between proteasomes and poly-GA ribbons are available at <https://github.com/anmartinez/poly-GA>.

The tomogram analyzed in [Figure 2](#) has been deposited at the Electron Microscopy Data Base with accession number EMDB: EMD-4191. The structures of the proteasome and TRiC/CCT obtained by *in situ* subtomogram averaging have been deposited at EMDB with the following accession numbers: EMDB: EMD-3916 (GS1 proteasome), EMD-3913 (GS2 proteasome), EMD-3914 (SPS1 proteasome), EMD-3915 (SPS2 proteasome), EMD-3917 (TRiC/CCT). The fitted atomic models of the different proteasome states have been deposited at the Protein Data Base with the following accession numbers: PDB: 6EPF (GS1), 6EPC (GS2), 6EPD (SPS1), 6EPE (SPS2).

Supplemental Figures

Cell

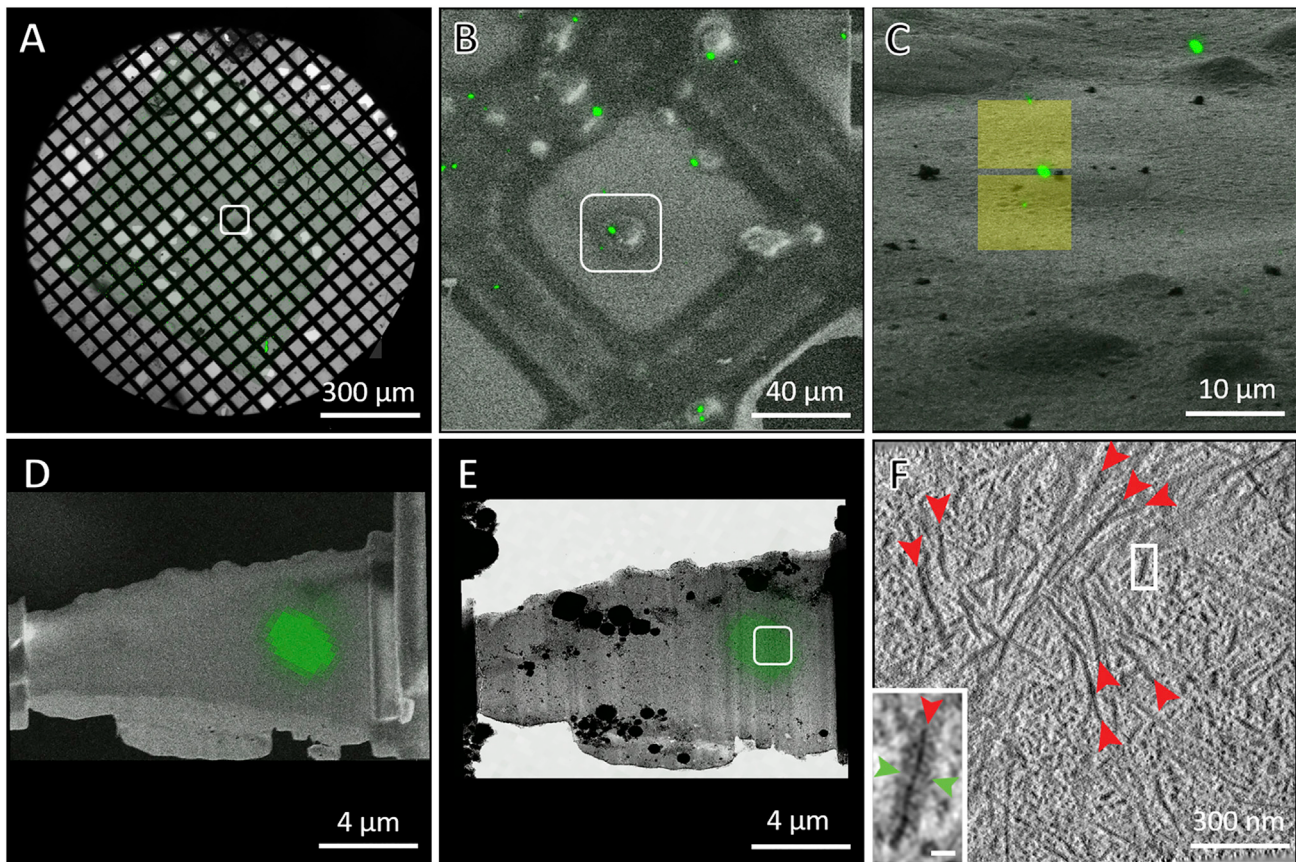


Figure S1. Correlative Cryo-light and Cryoelectron Microscopy Workflow, Related to Figure 1

(A) Rat cortical neurons were cultured on EM grids and transduced with (GA)₁₇₅-GFP on day 5. Upon vitrification by plunge freezing 5 days after transfection, the grids were imaged by cryo-light microscopy. (A) shows an overlay of phase and GFP channels.

(B) EM grids were transferred to a cryo-FIB/SEM microscope. To locate cells of interest (boxed), SEM images were aligned and superimposed with the GFP signal from the cryo-LM image.

(C) FIB-induced secondary electron image of the cell shown in (B), superimposed with the GFP signal. Yellow boxes mark the regions of the cell removed by FIB to produce a lamella containing the GFP-positive region.

(D) SEM image of the lamella resulting from FIB milling, with a final thickness of ~200 nm, superimposed with the GFP signal.

(E) Cryo-TEM low magnification image of the lamella shown in (D).

(F) 5 nm-thick tomographic slice of a tomogram recorded in the area marked by a white square in (E), containing the GFP signal. A dense network of poly-GA-GFP ribbons (red arrowheads) is visible. The inset shows a high magnification of a poly-GA-GFP ribbon decorated by GFP-associated additional densities (green arrowheads). Scale bar: 20 nm.

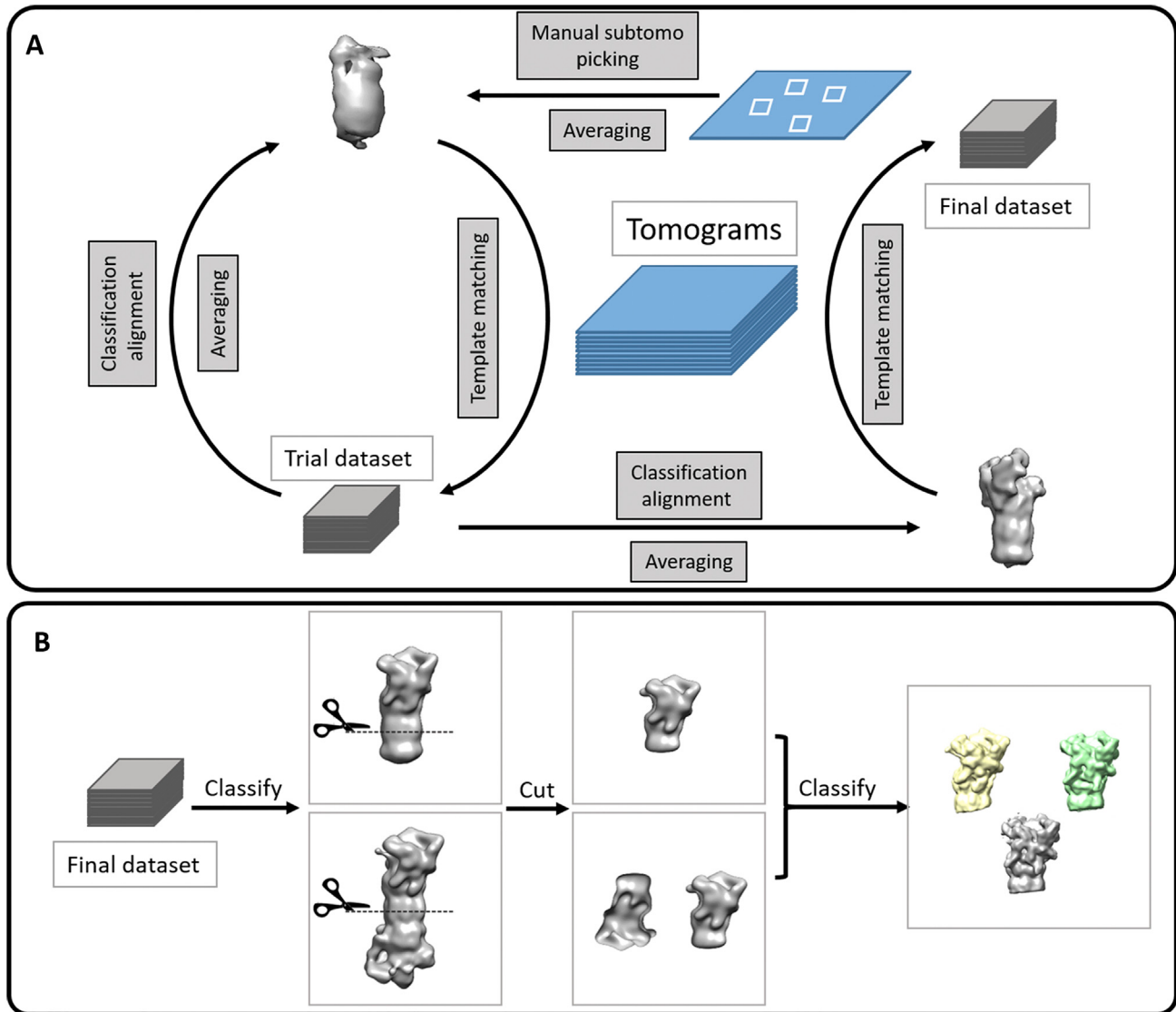


Figure S2. Subtomogram Averaging and Classification Workflow, Related to Figures 2 and 3

(A) Unbiased template matching procedure. Several identical structures were first hand-picked from one tomogram, aligned and averaged. The resulting average was used as a template to search more tomograms for additional occurrences of the same structure. These additional particles were then visually inspected, aligned, classified and averaged again to produce a higher resolution average. This average was low-pass filtered and used as a template to search all the tomograms to produce the final subtomogram dataset.

(B) All proteasome subtomograms were first classified into single-capped or double-capped. To further analyze the conformational status of the regulatory particles, all the subtomograms were cut *in silico* between the β-rings of the core particle (Asano et al., 2015), resulting in two independent particles for double-capped proteasomes. Cut out caps from all proteasomes were merged and subjected to a further round of classification.

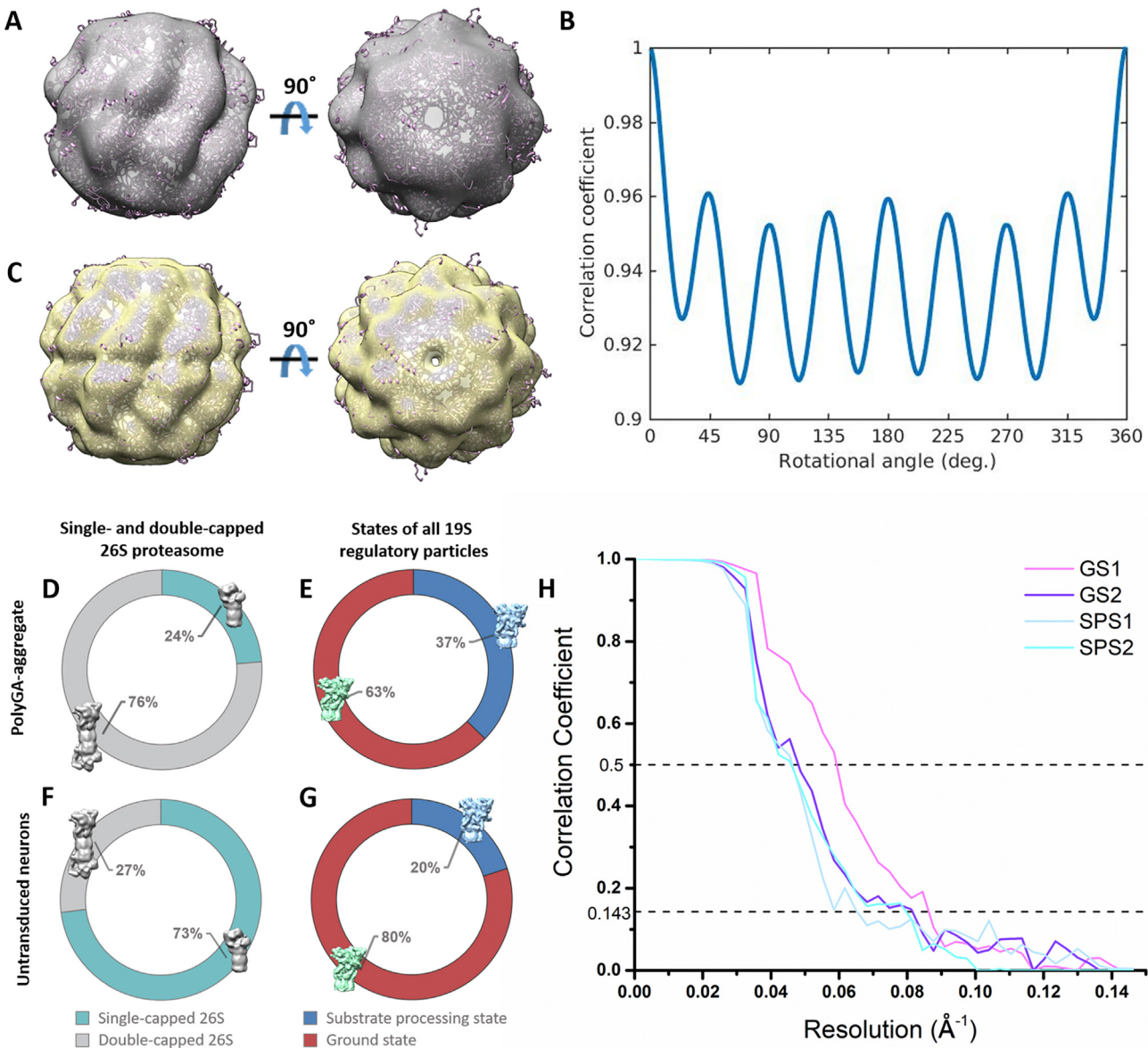


Figure S3. Subtomogram Averaging and Classification for TRiC/CCT and the 26S Proteasome, Related to Figures 2 and 3

(A) Unsymmetrized average structure of TRiC/CCT at a resolution of 20.5 Å superimposed on its atomic model (purple; PDB: 4V94).

(B) Rotational correlation coefficient analysis of (A) indicating 8-fold symmetry.

(C) Average structure of TRiC/CCT at a resolution of 17.1 Å upon application of D8 symmetry to (A) superimposed on its atomic model. Resolutions were estimated by gold-standard Fourier shell correlation using the 0.143 criterion.

(D and F) Overall distribution of single-capped and double-capped 26S proteasomes within aggregates in (GA)₁₇₅-GFP transduced neurons (D) and untransduced neurons (Asano et al., 2015) (F).

(E and G) Distribution of the ground and substrate processing states for all regulatory particles within aggregates in neurons transduced with (GA)₁₇₅-GFP (E) and untransduced (Asano et al., 2015) (G).

(H) Gold-standard Fourier shell correlation curves of the four proteasome structures, yielding the following resolution estimations: 11.8 Å (GS1), 12.3 Å (GS2), 15.4 Å (SPS1) and 12.8 Å (SPS2).

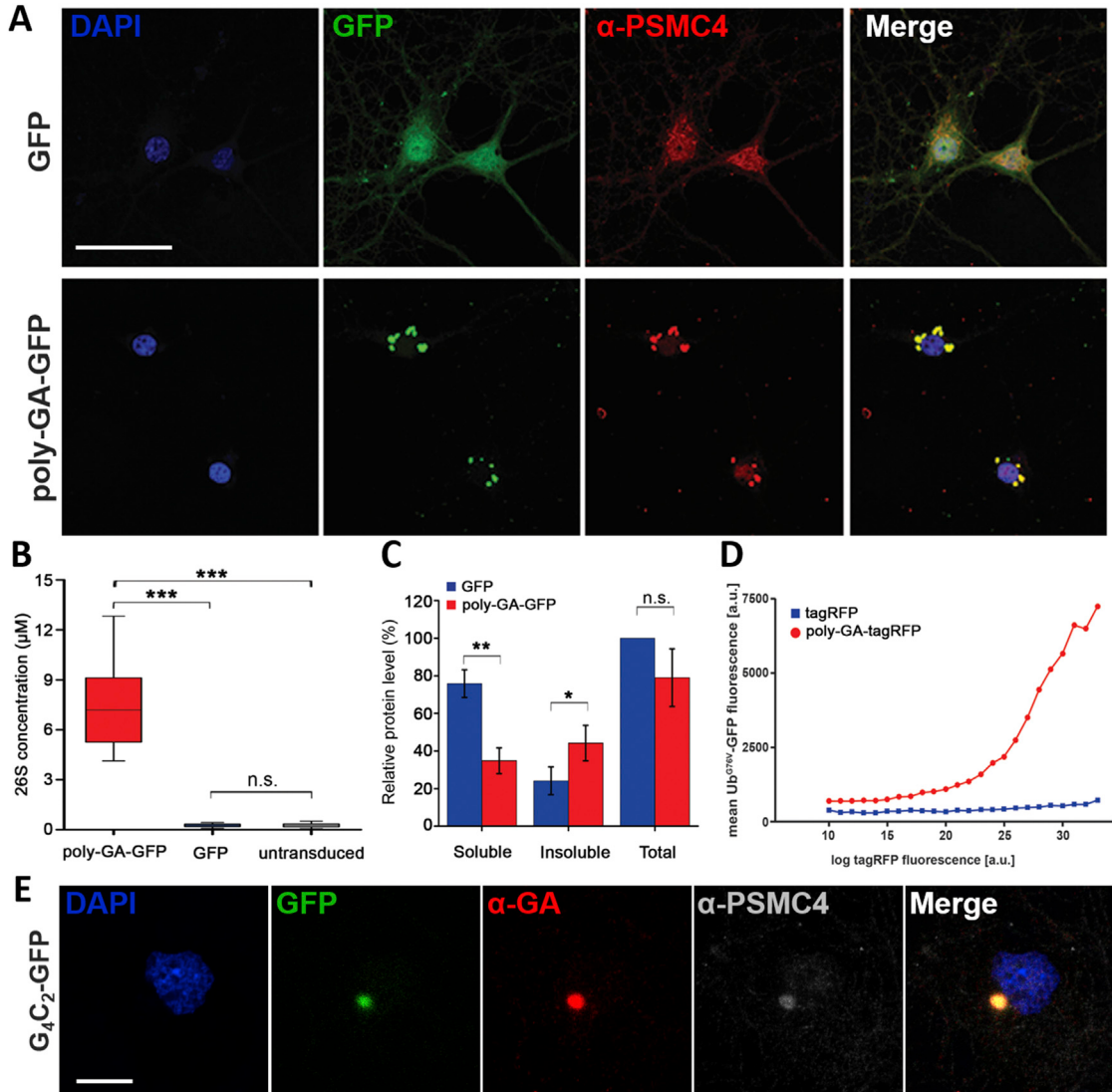


Figure S4. Proteasome Abundance and Function at Poly-GA Aggregates, Related to Figures 2 and 5

(A) Poly-GA-GFP aggregates (green) in primary neurons expressing a synthetic $(\text{GA})_{175}\text{-GFP}$ construct with a start codon colocalize with proteasomes detected with a PSMC4/Rpt3 antibody (red). Proteasome staining is diffuse in GFP-expressing control cells. Nuclei are labeled with DAPI (blue). Scale bar: 50 μm .

(B) Proteasome concentration for $(\text{GA})_{175}\text{-GFP}$ aggregates (DIV 5 + 5), control neurons transduced with GFP only (DIV 5 + 5) or untransduced (DIV 10) ($n = 9$ tomograms, $(\text{GA})_{175}\text{-GFP}$; $n = 17$, GFP; $n = 16$, untransduced). For poly-GA aggregates, only tomograms with more than half volume occupied by aggregates were considered for the concentration calculation. The top and bottom boundaries of the boxes indicate $\pm 2x$ standard error, and whiskers extend to the maximum and minimum values. Proteasome concentration within poly-GA aggregates was significantly higher than in control conditions (** $p < 0.001$ by Mann-Whitney test), whereas the difference between GFP-transfected and untransfected control neurons was not significant (n. s.).

(C) Quantification of proteasome levels in the soluble and insoluble fractions as well as total, analyzed by immunoblotting. The data was normalized to the total proteasome levels in GFP-transduced control neurons. Error bars indicate standard error. * and ** indicate respectively $p < 0.05$ and $p < 0.01$ by paired t test ($n = 6$ replicates from 4 independent experiments). Proteasomes are enriched in the insoluble fraction in the presence of poly-GA aggregates.

(D) Poly-GA expression leads to the stabilization of a reporter for the ubiquitin-proteasome system. HEK293 cells stably expressing an unstable green fluorescent reporter for the ubiquitin-proteasome system (UbG76V-GFP) were transfected with the indicated constructs. After 72 h, UbG76V-GFP levels were analyzed by flow cytometry. The relationship between poly-GA-tagRFP levels on the x axis and of UbG76V-GFP on the y axis shows a concentration-dependent accumulation of UbG76V-GFP in the presence of poly-GA. The data shown are from a single representative experiment out of three independent repeats.

(E) Poly-GA-GFP aggregates (green) in primary neurons expressing a non-ATG ($\text{G}_4\text{C}_2\text{)}_{73}$ construct containing a downstream GFP in the poly-GA reading frame. RAN translation-derived poly-GA-GFP aggregates are stained by a poly-GA antibody (red) and colocalize with proteasomes detected with a PSMC4/Rpt3 antibody (white). Nuclei are labeled with DAPI (blue). Scale bar: 10 μm .

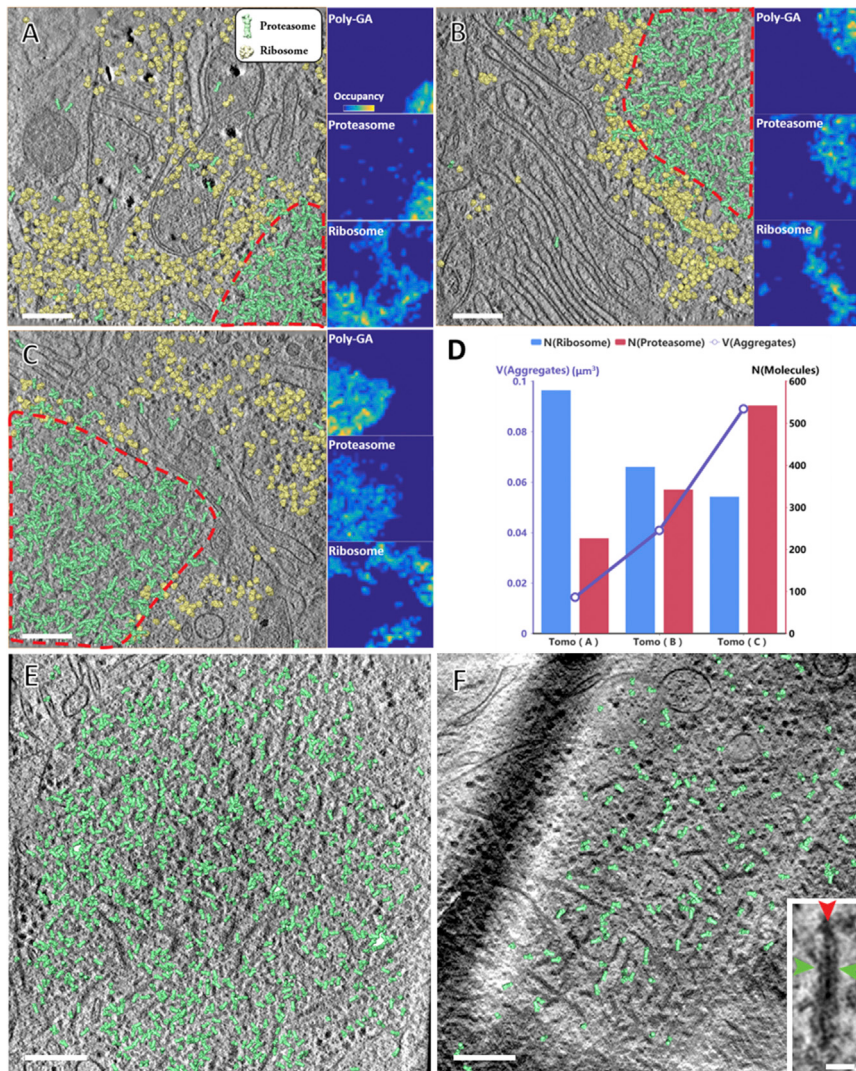


Figure S5. Macromolecule Mapping in Different Poly-GA Aggregates, Related to Figure 2

(A–C) Tomographic slices of aggregates within neurons transduced with $(\text{GA})_{175}\text{-GFP}$ (main panels) and analyzed at DIV 5 + 5. Regions containing poly-GA ribbons are outlined in red. For the whole tomogram, proteasomes (green) and ribosomes (yellow) are mapped to their original positions and orientations by template matching and subtomogram averaging. For each tomogram, maximum intensity projection heatmaps of poly-GA ribbons, proteasomes and ribosomes were generated (right column of each panel).

(D–F) Numbers of proteasomes and ribosomes detected in the tomograms shown in (A)–(C) plotted versus the volume of the region containing poly-GA aggregates. The number of proteasomes detected shows a positive correlation with poly-GA aggregate volume. (E and F) Tomographic slices and mapped 26S proteasomes of aggregates within neurons transduced with $(\text{GA})_{175}\text{-GFP}$ at an earlier time point (DIV 5 + 3) (E), or transfected with a RAN-translated $(\text{G}_4\text{C}_2)_{73}$ construct with GFP in the poly-GA reading frame (F). Note that despite the smaller size compared to DIV 5 + 5 $(\text{GA})_{175}\text{-GFP}$ aggregates, similar concentrations of proteasomes accumulated within these aggregates ($\sim 7 \mu\text{M}$ for $(\text{GA})_{175}\text{-GFP}$, DIV 5 + 3; $\sim 5 \mu\text{M}$ for G_4C_2). Due to the lower thickness of the cryo-FIB lamella (70 nm versus 100–200 nm in all other cases) fewer proteasomes are visible in (F). The inset in (F) shows a high magnification of a poly-GA ribbon (red arrowhead) decorated by GFP-associated additional densities (green arrowheads). Note that the morphology of RAN-translated poly-GA ribbons is indistinguishable from aggregates formed by the $(\text{GA})_{175}\text{-GFP}$ construct. Tomographic slices are 7 nm thick. Scale bars: 200 nm in main panels, 20 nm in inset.